Embedding Active Force Control within the Compliant Hybrid Zero Dynamics to Achieve Stable, Fast Running on MABEL

Koushil Sreenath, Hae-Won Park, Ioannis Poulakakis, J. W. Grizzle

***Abstract*—A mathematical formalism for designing running gaits in bipedal robots with compliance is introduced and subsequently validated experimentally on MABEL, a planar biped that contains springs in its drivetrain. The methods of virtual constraints and hybrid zero dynamics are used to design a time-invariant feedback controller that respects the natural compliance of the open-loop system. In addition, it also enables active force control within the compliant hybrid zero dynamics allowing within-stride adjustments of the effective stance leg stiffness. The proposed control strategy was implemented on MABEL and resulted in a kneed-biped running record of 3.06 m/s (10.9 kph or 6.8 mph).**

***Index Terms*—Bipedal robots, Running, Hybrid Systems, Zero Dynamics, Compliance, Force Control.**

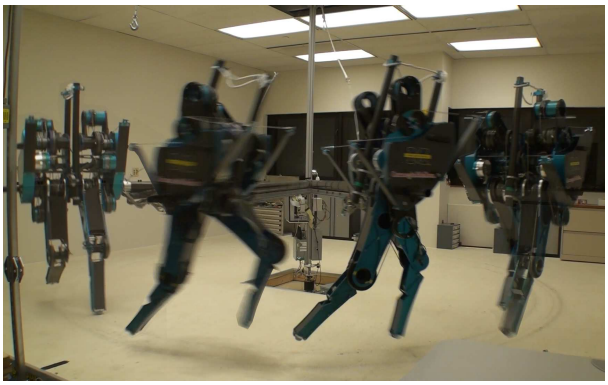

Fig. 1. A composite illustrating the dynamic and agile running gait obtained on MABEL.

I. Introduction

High-performance robot running requires the tight integration of the robot's mechanical and control systems. Successful running machines involve compliant elements—such as springs—which, combined with the hybrid underactuated nature of their dynamics and the small time intervals available for control, present a challenge to state-of-the-art feedback design approaches. In this article, we provide a method that combines the analytical tractability afforded by the hybrid zero dynamics framework, with physically intuitive compliance control to induce reliable, fast running gaits on the bipedal robot MABEL, obtaining speeds up to 3.06 m/s in physical laboratory experiments; see Figure 1.

Empirical controllers assisted from intuition gained through the analysis of simplified spring-mass models have been successful in stabilizing running on legged machines with particular morphology. Raibert and his collaborators in the 1980s introduced a set of simple, intuitive principles to make various one-foot gaits possible on monopedal, bipedal, and—through the concept of virtual legs—on quadrupedal robots; (Raibert, 1986). The proposed controllers regulate forward velocity by suitably positioning the legs during flight, and regulate hopping height and torso pitch by making use of motor torques during stance. These controllers have achieved record speeds up to 5.9 m/s on a monopedal hopper (Koechling, 1989).

The success of Raibert's control procedures prompted a series of robots (Sayyad et al., 2007), and mathematical models (Holmes et al., 2006), to investigate a variety of design and control aspects of robot running, including self-stability (Ghigliazza et al., 2003), energy minimization (Ahmadi and Buehler, 1997, 2006), active force control (Koepl et al., 2010), and energy removal strategies (Andrews et al., 2011). The majority of these systems are monopedal and feature light, prismatic, springy legs that are typically connected to the robot's torso so that the hip joint coincides with the torso's center of mass. It is not clear, however, how control methods developed in the context of such systems can be transferred to robots whose morphology departs significantly from these assumptions. In particular, bipedal robots—such as MABEL, Figure 1—whose legs comprise revolute knee joints and have significant weight, and are coupled nontrivially to the torso dynamics represent a challenge to control approaches derived on the basis of Raibert-style hoppers.

Contrary to walking gaits—for which a variety of controllers with analytically tractable properties are available; see (Spong, 1999; Chevallereau et al., 2003; Ames

Koushil Sreenath and J. W. Grizzle are with the Control Systems Laboratory, Electrical Engineering and Computer Science Department, University of Michigan, Ann Arbor, MI 48109-2122, USA. {koushils, grizzle}@umich.edu

Hae-Won Park is with the Mechanical Engineering Department, University of Michigan, Ann Arbor, MI 48109-2125, USA. parkhw@umich.edu

Ioannis Poulakakis is with the Mechanical Engineering Department, University of Delaware, Delware. poulakas@udel.edu

This work is supported in part by NSF grants ECS-909300 and CMMI-1130372, and in part by DARPA Contract W91CRB-11-1-0002.

et al., 2006; Gregg and Spong, 2010) for instance—only few control methods are available for running bipeds. In many cases, running was implemented on robots that were not specifically designed for such motions. Examples include humanoids like Sony's QRIO (Nagasaka et al., 2004), Honda's ASIMO (Hirose and Ogawa, 2007), the HRP family (Kajita et al., 2005, 2007), and HUBO (Cho et al., 2009). Recently, Toyota's humanoid achieved running at speeds up to 1.94 m/s (Tajima et al., 2009). In all these cases, the underlying controllers are based on the Zero Moment Point (ZMP) criterion for stability, and the resulting running gaits exhibit short flight durations and low ground clearance during flight.

A quite different paradigm for control law design has been employed to induce running on RABBIT, a planar biped with revolute knees and rigid links, (Morris et al., 2006). According to this framework, running gaits are "embedded" in the dynamics of the robot through a set of holonomic output functions which are driven to zero by its actuators; see (Westervelt et al., 2007) for a detailed overview of the method. Although running with significant flight duration and good ground clearance was successfully realized, it could not be sustained for more than six steps. Failure to maintain running in RABBIT was a consequence of its lack of compliance combined with the limitations of its actuators.

Elastic energy storage in compliant elements is of central importance in explaining the mechanics of running, (Alexander, 1990; McMahon and Cheng, 1990), and is indispensable for the realization of running in legged robots (Raibert, 1986; Hurst and Rizzi, 2008). In particular, springs can store—in the first part of stance, as the leg contracts—and then release—in the second part of stance, when the leg extends—part of the energy needed to redirect the center of mass (COM) of the robot upwards prior to the flight phase. In the absence of springs, the actuators would have to perform negative work on impact and then supply the energy required for flight. These considerations motivated the design of MABEL, a planar bipedal robot, which incorporates compliant elements for both energy efficiency and shock absorption.

The presence of compliance, however, poses strict requirements on the control system, which must work in concert with the springs of the open-loop system to achieve closed-loop stability. To design feedback control laws that take advantage of compliant elements, the notion of *compliant hybrid zero dynamics* was introduced in (Poulakakis, 2008). The proposed method organizes the robot around a lower-dimensional physically-compliant mechanical system—the Spring Loaded Inverted Pendulum (SLIP)—which governs the closed-loop dynamics of the higher-dimensional system (Poulakakis and Grizzle, 2009b). The method was extended in (Poulakakis and Grizzle, 2009a) to induce hopping motions on the monopedal robot Thumper—a single-legged version of MABEL—and was further refined in (Sreenath et al., 2011b) to produce dynamically stable walking motions experimentally on MABEL, where the designed controller preserved the natural compliant dynamics in the closed-loop ensuring the compliance performs the negative work at impact and thereby resulting in energy efficient walking gaits. The nonlinear compliant hybrid zero dynamics controller implemented on MABEL was instrumental in obtaining fast walking at a top sustained speed of 1.5 m/s (3.4 mph.)

The notion of compliant hybrid zero dynamics is central to controlling running on MABEL. However, contrary to walking motions, running is typically characterized by the presence of flight phases (McMahon et al., 1987), during which only limited control authority can be exercised over the system. In fact, MABEL spends approximately 40% of its running cycle in flight, leaving about 200 ms per stride for the stance phase, during which control over the system's total energy and torso motion can be exerted. The duration of the stance phase can be effectively regulated through adjusting the leg stiffness. For example, reducing the stiffness of the leg springs can extend the stance phase duration, thereby offering enhanced control capability in continuous time through the robot's actuators. However, as was observed in (Rummel and Seyfarth, 2008) in running with segmented legs that employ compliant revolute knee joints, reducing the leg stiffness can cause the robot to collapse at moderate leg compressions. Particularly in MABEL, which weighs 65 Kg, extending the stance duration by reducing leg stiffness results in the leg collapsing, raising the need for effective leg compliance adjustment policies to achieve reliable highly-dynamic running motions.

Leg stiffness adaptation strategies have been studied extensively in the context of biomechanics. For instance, it is known that human runners adjust their leg stiffness to maintain similar peak ground reaction forces and contact times on ground surfaces with different properties (Ferris and Farley, 1997; Ferris et al., 1998). Further, through experiments on running guinea fowl encountering unexpected terrain drops, (Daley et al., 2006; Daley and Biewener, 2006) demonstrate that large perturbations up to 40% of their hip height can be handled by changing leg stiffness. Motivated by these experiments, an active force control strategy has been suggested in (Koepl et al., 2010) and an active energy removal controller has been proposed in (Andrews et al., 2011) to enhance the robustness of single-leg hoppers to perturbations in ground height and ground stiffness.

In this article, we combine stiffness adaptation through active force control with dimensional reduction through motion control to introduce a family of model-based feedback controllers that induce reliable fast running gaits on compliant bipedal robots with revolute knee joints. The proposed control laws act in both continuous and discrete time to impose a set of suitably parameterized virtual holonomic constraints that reduce the higher-dimensional robot dynamics to a lower-dimensional hybrid dynamical system—the hybrid zero dynamics (HZD)—which not only respects the open-loop leg com-

pliance, but also effectively tunes it throughout the gait to enhance the robustness of the controller to perturbations in the knee angle at impact. Local stability analysis via Poincaré's method reveals that the resulting closed-loop system is exponentially stable. This controller is implemented on MABEL, both with passive feet (no ankle actuation) and with point feet, to realize stable running motions. With the passive feet, running was realized at an average speed of 1.07 m/s, while with point feet, running was realized at an average speed of 1.95 m/s and a peak speed of 3.06 m/s. About 40% of the gait was spent in flight, with estimated peak ground clearance of 7 to 10 cms. Figure 1 illustrates a composite image of the running gait for MABEL.

The remainder of the paper is organized as follows. Section II presents a hybrid model for running that will be used for controller design. Section III gives an overview of the control design with Section IV providing implmentation details for achieving exponentially stable and robust running gaits. Section V describes the experiments performed to demonstrate the validity of the designed controller. Finally Section VI provides concluding remarks.

II. MABEL Model

A. Description of MABEL

MABEL is a planar bipedal robot that is used as a testbed for experimental validation of walking and running controller designs. Its comprised of five links assembled to form a torso and two legs with knees; see Figure 1. The robot weighs 65 kg, has 1 m long legs, and is mounted on a boom of radius 2.25 m. The legs are terminated in point feet. All actuators are located in the torso, so that the legs are kept as light as possible; this is to facilitate rapid leg swinging for running. Unlike most bipedal robots, the actuated degrees of freedom of each leg do not correspond to the knee and hip angles. Instead, for each leg, a collection of cable-differentials is used to connect two motors to the hip and knee joints in such a way that one motor controls the angle of the virtual leg (henceforth called the leg angle) consisting of the line connecting the hip to the toe, and the second motor is connected in series with a spring in order to control the length or shape of the virtual leg (henceforth called the leg shape); see Figure 2. Table III provides a glossary of symbols used in the paper. More details on the design of MABEL can be found at (Park et al., 2011; Grizzle et al., 2009; Hurst, 2008).

Springs in MABEL appear *in series* with an actuator. They serve to isolate the reflected rotor inertia of the leg-shape motors from the impact forces at leg touchdown and to store energy in the compression phase of a running gait, when the support leg must decelerate the downward motion of the robot's center of mass; the energy stored in the spring can then be used to redirect the center of mass upwards for the subsequent flight phase. These properties (shock isolation and energy storage) enhance the energy efficiency of running and reduce the overall actuator power requirements. MABEL has a unilateral spring which compresses but does not extend beyond its rest length. This ensures that springs are present when they are useful for shock attenuation and energy storage, and absent when they would be a hindrance for lifting the legs from the ground.

The following sections will develop the hybrid model appropriate for a running gait comprised of continuous phases representing stance and flight phases of running, and discrete transitions between the two.

B. MABEL's Unconstrained Dynamics

The configuration space Q_{e} of the unconstrained (or extended) dynamics of MABEL is nine dimensional: five DOF are associated with the links in the robot's body, two DOF are associated with the springs in series with the two leg-shape motors, and two DOF are associated with the horizontal and vertical position of the robot in the sagittal plane. A set of coordinates suitable for parametrization of the robot's linkage and transmission is, $q_{\mathrm{e}} := (\ q_{\mathrm{LA_{st}}};\ q_{\mathrm{mLS_{st}}};\ q_{\mathrm{Bsp_{st}}};\ q_{\mathrm{LA_{sw}}};\ q_{\mathrm{mLS_{sw}}};\ q_{\mathrm{Bsp_{sw}}};\ q_{\mathrm{Tor}};\ p^h_{\mathrm{hip}};\ p^v_{\mathrm{hip}}\ )$. From Table III and the angles illustrated in Figure 2(b), q_{Tor} is the torso angle, and $q_{\mathrm{LA_{st}}}$, $q_{\mathrm{mLS_{st}}}$, and $q_{\mathrm{Bsp_{st}}}$ are the leg angle, leg-shape motor position and $\mathrm{B}_{\mathrm{spring}}$ position respectively for the stance leg. The swing leg variables, $q_{\mathrm{LA_{sw}}}$, $q_{\mathrm{mLS_{sw}}}$ and $q_{\mathrm{Bsp_{sw}}}$ are defined similarly. For each leg, q_{LS} is uniquely determined by a linear combination of q_{mLS} and q_{Bsp}, reflecting the fact that the cable differentials place the spring in series with the motor, with the pulleys introducing a gear ratio. The coordinates $p^h_{\mathrm{hip}}, p^v_{\mathrm{hip}}$ are the horizontal and vertical positions of the hip in the sagittal plane.

The method of Lagrange is employed to obtain the equations of motion. In computing the Lagrangian, the total kinetic energy is taken to be the sum of the kinetic energies of the transmission, the rigid linkage, and the boom. The potential energy is computed in a similar manner with the difference being that the transmission contributes to the potential energy of the system only through its gravitational potential energy. This distinction is made since it is more convenient to model the unilateral spring as an external input to the system. The resulting model of the robot's unconstrained dynamics is determined as

$$D_{\mathrm{e}}(q_{\mathrm{e}})\,\ddot{q}_{\mathrm{e}} + C_{\mathrm{e}}(q_{\mathrm{e}},\dot{q}_{\mathrm{e}})\,\dot{q}_{\mathrm{e}} + G_{\mathrm{e}}(q_{\mathrm{e}}) = \Gamma_{\mathrm{e}}, \qquad (1)$$

where, D_{e} is the inertia matrix, C_{e} contains Coriolis and centrifugal terms, G_{e} is the gravity vector, and Γ_{e} is the vector of generalized forces acting on the robot, expressed as,

$$\begin{aligned}\Gamma_{\mathrm{e}} = {} & B_{\mathrm{e}}u + E_{\mathrm{ext}}(q_{\mathrm{e}})\,F_{\mathrm{ext}} + \\ & B_{fric}\tau_{fric}(q_{\mathrm{e}},\dot{q}_{\mathrm{e}}) + B_{sp}\tau_{sp}(q_{\mathrm{e}},\dot{q}_{\mathrm{e}}),\end{aligned} \qquad (2)$$

where the matrices B_{e}, E_{ext}, B_{fric}, and B_{sp} are derived from the principle of virtual work and define how the

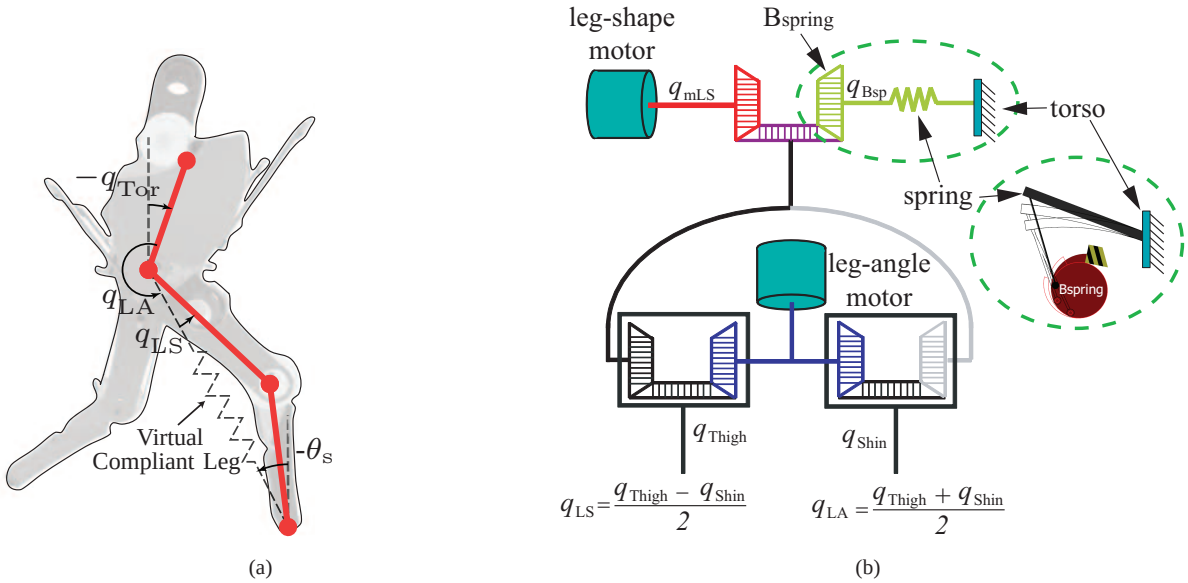

Fig. 2. (a) The *virtual compliant leg* created by the drivetrain through a set of differentials. The coordinate system used for the linkage is also indicated. Angles are positive in the counter clockwise direction. (b) MABEL's drivetrain (same for each leg), all housed in the torso. Two motors and a spring are connected to the traditional hip and knee joints via three differentials. On the robot, the differentials are realized via cables and pulleys (Hurst, 2008) and not via gears. They are connected such that the actuated variables are leg angle and leg shape, so that the spring is in series with the leg shape motor. The base of the spring is grounded to the torso and the other end is connected to the $\mathrm{B}_{\mathrm{spring}}$ differential via a cable, which makes the spring *unilateral*. When the spring reaches its rest length, the pulley hits a hardstop, formed by a very stiff damper. When this happens, the leg shape motor is, for all intents and purposes, rigidly connected to leg shape through a gear ratio.

actuator torques u, the external forces F_{ext} at the leg, the joint friction forces τ_{fric}, and the spring torques τ_{sp} enter the model respectively. The dimension of u is four, corresponding to the two brushless DC motors on each leg for actuating leg shape and leg angle.

C. MABEL's Constrained Dynamics

The model (1) can be particularized to describe the stance and flight dynamics by incorporating proper holonomic constraints.

1) Dynamics of Stance: For modeling the stance phase, the stance toe is assumed to act as a passive pivot joint (no actuation, no slip, and no rebound.) Thus, the coordinates of the stance leg and torso define the Cartesian position of the hip, $\left(p^h_{\mathrm{hip}}, p^v_{\mathrm{hip}}\right)$. The springs in the transmission are appropriately chosen so that they are stiff enough to support the entire weight of the robot. Consequently, it is assumed that the spring on the swing leg does not deflect, that is, $q_{\mathrm{Bsp}_{\mathrm{sw}}} \equiv 0$. The stance configuration space, Q_{s}, is therefore a co-dimension three submanifold of Q_{e}. With these assumptions, the generalized configuration variables in stance are taken as $q_{\mathrm{s}} := \left(q_{\mathrm{LA}_{\mathrm{st}}}; q_{\mathrm{mLS}_{\mathrm{st}}}; q_{\mathrm{Bsp}_{\mathrm{st}}}; q_{\mathrm{LA}_{\mathrm{sw}}}; q_{\mathrm{mLS}_{\mathrm{sw}}}; q_{\mathrm{Tor}}\right)$. Defining the state vector $x_{\mathrm{s}} := (q_{\mathrm{s}}; \dot{q}_{\mathrm{s}}) \in TQ_{\mathrm{s}}$, where TQ_{s} is the tangent bundle of Q_{s}, the stance dynamics can be expressed in standard form as,

$$\dot{x}_{\mathrm{s}} = f_{\mathrm{s}}(x_{\mathrm{s}}) + g_{\mathrm{s}}(x_{\mathrm{s}})u. \tag{3}$$

2) Dynamics of Flight: In the flight phase, both feet are off the ground, and the robot follows a ballistic motion under the influence of gravity. Thus the flight dynamics can be modeled by the unconstrained dynamics developed earlier. However in order to eliminate the stiffness in integrating the differential equations representing the flight model, an additional assumption can be made. Since the springs are stiff enough to support the entire weight of the robot, during flight when the feet are off the ground, it can be assumed that the springs are at their rest position and do not deflect[1]. Therefore, $q_{\mathrm{Bsp}_{\mathrm{st}}} \equiv 0, q_{\mathrm{Bsp}_{\mathrm{sw}}} \equiv 0$. Thus, the configuration space of the flight dynamics is a co-dimension two submanifold of Q_{e}, i.e., $Q_{\mathrm{f}} := \left\{q_{\mathrm{e}} \in Q_{\mathrm{e}} \mid q_{\mathrm{Bsp}_{\mathrm{st}}} \equiv 0, q_{\mathrm{Bsp}_{\mathrm{sw}}} \equiv 0\right\}$. It follows that the generalized configuration variables in the flight phase can be taken as $q_{\mathrm{f}} := \left(q_{\mathrm{LA}_{\mathrm{st}}}; q_{\mathrm{mLS}_{\mathrm{st}}}; q_{\mathrm{LA}_{\mathrm{sw}}}; q_{\mathrm{mLS}_{\mathrm{sw}}}; q_{\mathrm{Tor}}; p^h_{\mathrm{hip}}; p^v_{\mathrm{hip}}\right)$. Defining the state vector $x_{\mathrm{f}} := (q_{\mathrm{f}}; \dot{q}_{\mathrm{f}}) \in TQ_{\mathrm{f}}$, where TQ_{f} is the tangent bundle of Q_{f}, the flight dynamics can be expressed in standard form as,

$$\dot{x}_{\mathrm{f}} = f_{\mathrm{f}}(x_{\mathrm{f}}) + g_{\mathrm{f}}(x_{\mathrm{f}})u. \tag{4}$$

D. MABEL's Transitions

1) Stance to Flight Transition Map: Physically, the robot takes off when the normal component of the ground reaction force acting on the stance toe, $F^N_{toe_{\mathrm{st}}}$, becomes zero. The ground reaction force at the stance toe can be computed as a function of the acceleration of the COM and thus depends on the inputs $u \in \mathcal{U}$

[1]The pre-tension in the cables between the spring and the pulley $\mathrm{B}_{\mathrm{spring}}$ (see Figure 2(b)) has been set as close to zero as possible to ensure the spring is not pre-loaded.

of the system described by (3). Mathematically, the transition occurs when the solution of (3) intersects the co-dimension one switching manifold

$$\mathcal{S}_{\mathrm{s}\to\mathrm{f}} := \left\{ x_{\mathrm{s}} \in TQ_{\mathrm{s}} \times \mathcal{U} \mid F^N_{toe_{\mathrm{st}}} = 0 \right\}. \tag{5}$$

On transition from the stance to flight phase, the stance leg comes off the ground and takeoff occurs. During the stance phase, the spring on the stance leg is compressed. When the stance leg comes off the ground, the spring rapidly decompresses and impacts the hard stop. The stance to flight transition map, $\Delta_{\mathrm{s}\to\mathrm{f}} : \mathcal{S}_{\mathrm{s}\to\mathrm{f}} \to TQ_{\mathrm{f}}$ accounts for this. Further details are omitted for the sake of brevity and interested readers are referred to (Sreenath, 2011, Chap. III).

2) Flight to Stance Transition Map: The robot physically transitions from flight phase to stance phase when the swing toe contacts the ground surface. The impact is modeled here as an inelastic contact between two rigid bodies. It is assumed that there is no rebound or slip at impact. Mathematically, the transition occurs when the solution of (4) intersects the co-dimension one switching manifold

$$\mathcal{S}_{\mathrm{f}\to\mathrm{s}} := \left\{ x_{\mathrm{f}} \in TQ_{\mathrm{f}} \mid p^v_{\mathrm{toe}_{\mathrm{sw}}} = 0 \right\}. \tag{6}$$

In addition to modeling the impact of the leg with the ground, and the associated discontinuity in the generalized velocities of the robot (Hürmüzlü and Chang, 1992), the transition map accounts for the assumption that the spring on the new swing leg remains at its rest length, and for the relabeling of the robot's coordinates so that only one stance model is necessary. In particular, the transition map $\Delta_{\mathrm{f}\to\mathrm{s}} : \mathcal{S}_{\mathrm{f}\to\mathrm{s}} \to TQ_{\mathrm{s}}$ consists of three subphases executed in the following order: (a) standard rigid impact model (Hürmüzlü and Chang, 1992); (b) adjustment of spring velocity in the new swing leg; and (c) coordinate relabeling.

E. Hybrid Control Design Model for Running

The hybrid model of running is based on the dynamics developed in Section II-C and the transition maps presented in Section II-D, and is given by

$$\Sigma_{\mathrm{s}} : \begin{cases} \dot{x}_{\mathrm{s}} = f_{\mathrm{s}}(x_{\mathrm{s}}) + g_{\mathrm{s}}(x_{\mathrm{s}})\, u, & (x^-_{\mathrm{s}}, u^-) \notin S_{\mathrm{s}\to\mathrm{f}} \\ x^+_{\mathrm{f}} = \Delta_{\mathrm{s}\to\mathrm{f}}\left(x^-_{\mathrm{s}}, u^-\right), & (x^-_{\mathrm{s}}, u^-) \in S_{\mathrm{s}\to\mathrm{f}} \end{cases}$$

$$\Sigma_{\mathrm{f}} : \begin{cases} \dot{x}_{\mathrm{f}} = f_{\mathrm{f}}(x_{\mathrm{f}}) + g_{\mathrm{f}}(x_{\mathrm{f}})\, u, & x^-_{\mathrm{f}} \notin S_{\mathrm{f}\to\mathrm{s}} \\ x^+_{\mathrm{s}} = \Delta_{\mathrm{f}\to\mathrm{s}}\left(x^-_{\mathrm{f}}\right), & x^-_{\mathrm{f}} \in S_{\mathrm{f}\to\mathrm{s}}. \end{cases} \tag{7}$$

F. Validation Model

The model developed in the previous sections will be used for control design. However, we note that the developed model does not capture the following aspects of the experimental testbed: (a) a compliant ground and the possibility of slipping; (b) stretchy cables in the transmission of the robot; and (c) dynamics of the boom. A *more detailed model* was developed in (Park et al., 2011) to capture these effects, however it is not computationally tractable for use in control design for running. Instead, we will design the controller based on the model developed here and then use the detailed model for validation of the controller prior to experimental deployment.

III. Control Design for Running

This section presents a controller for inducing stable running motions on MABEL. To do this, the controller creates an actuated compliant hybrid zero dynamics (HZD) that enables actively adjusting the effective leg stiffness during the stance phase. Details about the implementation of this controller are relegated to Section IV.

A. Overview of the Control Method

The control objective is to design exponentially stable running periodic gaits that are robust to perturbations, so as to accommodate inevitable differences between the model and the robot. To achieve this objective, the feedback introduces control on four levels; see Figure 3. On the first level, continuous-time feedback controllers Γ^{α}_{p} with $p \in \mathcal{P} := \{\mathrm{s}, \mathrm{f}\}$ are employed in the stance and flight phases to impose suitably parametrized virtual holonomic constraints that restrict the motion of the system on lower-dimensional invariant and attractive surfaces $\mathcal{Z}_{\alpha_p}$ embedded in the state space. On the second level, discrete-time feedback controllers $\Gamma^{\alpha_c}_{p}$ are employed at transitions between the stance and flight phases to render the surfaces $\mathcal{Z}_{\alpha_p}$ hybrid invariant (Westervelt et al., 2007). The system in closed-loop with the controllers Γ^{α}_{p} and $\Gamma^{\alpha_c}_{p}$ admits a well defined hybrid zero dynamics that governs the stability properties of the higher-dimensional robot plant.

The outer-loop controller Γ^{β} renders the hybrid zero dynamics locally exponentially stable by updating certain parameters from stride to stride. We introduce an additional outer-loop controller Γ^{γ} to enhance the robustness of the controller to unexpected uncertainty in parameters in the robot and the environment; in particular, perturbations in the knee angle at impact and imperfections in the ground contact model.

The novelty of the controller lies in that the feedback not only preserves the natural compliance of the open-loop system as a dominant characteristic of its closed-loop behavior, but also introduces active force control as a means of varying the effective compliance of the stance leg.

The remaining parts of this section will more fully describe the key portions of the control law. As noted previously, certain technical details are saved for Section IV which can be skipped for the first reading of the manuscript.

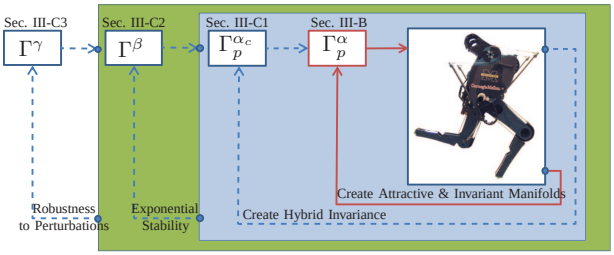

Fig. 3. Feedback diagram illustrating the running controller structure. Continuous lines represent signals in continuous time; dashed lines represent signals in discrete time. The controllers Γ_p^{α} and $\Gamma_p^{\alpha_c}$ create a compliant actuated hybrid zero dynamics. The controller Γ^{β} ensures that the periodic orbit on the resulting zero dynamics manifold is locally exponentially stable. The controller Γ^{γ} increases the robustness to perturbations in the knee angle at impact and to imperfections in the ground contact model.

B. Continous-time Control

1) Motion Control: The motion controller asymptotically imposes a set of virtual holonomic constraints through feedback. Its purpose is to synchronize the links of the robot to achieve common objectives in running, such as supporting the torso, advancing the swing leg in relation to the stance leg, and specifying foot clearance. Virtual constraints can be expressed in the form of an output, that when zeroed by a feedback controller, enforces the constraint. For each phase $p \in \mathcal{P}$ in running, the virtual constraints can then be expressed in the form

$$y_p = h_p\left(q_p, \alpha_p\right) = H_0^p q_p - h_d^p\left(\theta_p, \alpha_p\right). \tag{8}$$

Here H_0^p represents a selection matrix, and $H_0^p q_p$ represents the controlled variables, corresponding to a linear combination of the configuration variables; h_d^p is the desired evolution that is described through Bézier polynomials parametrized by a strictly monotonic function of the joint configuration variables, θ_p, whose physical meaning will be specified in Section IV; and α_p are coefficients of the Bézier polynomials. In implementing the controller, one can choose the controlled variables by selecting H_0^p and their corresponding desired evolution by selecting α_p in (8).

To enforce the constraints, the objective of the actuators is to zero the output defined by (8). Following (Isidori, 1995), we differentiate the output twice with respect to time, obtaining,

$$\frac{d^2 y_p}{dt^2} = L_{f_p}^2 h_p\left(x_p, \alpha_p\right) + L_{g_p} L_{f_p} h_p\left(q_p, \alpha_p\right) u_p, \tag{9}$$

where $L_{g_p} L_{f_p} h_p\left(q_p, \alpha_p\right)$ is the decoupling matrix. Under the conditions of (Westervelt et al., 2007, Lemma 5.1), the decoupling matrix has full rank, and

$$\begin{aligned} u_p^*\left(x_p, \alpha_p\right) := &- \left(L_{g_p} L_{f_p} h_p\left(q_p, \alpha_p\right)\right)^{-1} \\ &L_{f_p}^2 h_p\left(x_p, \alpha_p\right), \end{aligned} \tag{10}$$

is the unique control input that renders the surface

$$\begin{aligned} \mathcal{Z}_{\alpha_p} = \{&x_p \in TQ_p \mid h_p\left(q_p, \alpha_p\right) = 0, \\ &L_{f_p} h_p\left(x_p, \alpha_p\right) = 0\} \end{aligned} \tag{11}$$

invariant under the continuous dynamics for $p \in \mathcal{P}$, i.e., for every $z_p \in \mathcal{Z}_{\alpha_p}$, $f_p^*\left(z_p\right) := f_p\left(z_p\right) + g_p\left(z_p\right) u_p^* \in T_{z_p} \mathcal{Z}_{\alpha_p}$. Zeroing the outputs effectively reduces the dimension of the system by restricting its dynamics on the surface $\mathcal{Z}_{\alpha_p}$, which is called the zero dynamics manifold. The dynamics of the system restricted on $\mathcal{Z}_{\alpha_p}$,

$$\dot{z}_p = f_p^*|_{\mathcal{Z}_{\alpha_p}}\left(z\right),$$

is called the zero dynamics. To achieve attractivity of $\mathcal{Z}_{\alpha_p}$, the controller (10) is modified as

$$\begin{aligned} u_p = &u^*\left(x_p, \alpha_p\right) - \left(L_{g_p} L_{f_p} h_p\left(q_p, \alpha_p\right)\right)^{-1} \\ &\left(\frac{K_{p,P}}{\epsilon^2} y_c^p + \frac{K_{p,D}}{\epsilon} \dot{y}_c^p\right), \end{aligned} \tag{12}$$

where $\epsilon > 0$ is sufficiently small and $K_{p,P}, K_{p,D}$ are such that $\lambda^2 + K_{p,D}\lambda + K_{p,P} = 0$ is Hurwitz.

***Remark** 1:* A modification of this control scheme that will be useful in accommodating compliance tuning during stance is to reserve one of the actuators for active force control within the zero dynamics. In more detail, during the stance phase, where four actuators are available, we will engage only three to impose virtual holonomic constraints and reserve the stance leg shape motor, $u_{\mathrm{mLS_{st}}}$, as an input available for control within the zero dynamics. In this case, the continuous stance dynamics can be rewritten as

$$\dot{x}_{\mathrm{s}} = f_{\mathrm{s}}(x_{\mathrm{s}}) + \tilde{g}_{\mathrm{s}}(x_{\mathrm{s}})\tilde{u}_{\mathrm{s}} + g_{\mathrm{mLS_{st}}}(x_{\mathrm{s}})\ u_{\mathrm{mLS_{st}}},$$

where $\tilde{u}_{\mathrm{s}}$ are the actuators used to enforce virtual constraints. Then, the zero dynamics becomes

$$\dot{z}_p = f_p^*|_{\mathcal{Z}_{\alpha_p}}\left(z\right) + g_{\mathrm{mLS_{st}}}|_{\mathcal{Z}_{\alpha_p}}\left(z\right) u_{\mathrm{mLS_{st}}}. \tag{13}$$

2) Active Force Control: The explicit appearance of $u_{\mathrm{mLS_{st}}}$ input in the zero dynamics (13) allows us to use feedback to create a virtual compliant element. In particular, by defining the feedback

$$u_{\mathrm{mLS_{st}}}\left(x_{\mathrm{s}}\right) = -k_{\mathrm{vc}}\left(q_{\mathrm{mLS_{st}}} - q_{\mathrm{mLS_{vc}}}\right), \tag{14}$$

a virtual compliant element of stiffness k_{vc}, and rest position $q_{\mathrm{mLS_{vc}}}$ is implemented using the motor leg shape actuator. An additional damping element could be added if desired. The transmission of MABEL places this virtual compliant element in series with the physical compliance. Since both these compliances are in series, this method provides a means of dynamically varying the effective compliance of the system. For future use, note that, the existence of the virtual compliant element introduces a parameter vector $\alpha_{\mathrm{vc}} = (k_{\mathrm{vc}}, q_{\mathrm{mLS_{vc}}})$.

To provide some intuituion, virtual compliance facilitates energy injection to enable takeoff and effectively accounts for the softening of the leg spring as the knee bends, as observed in (Rummel and Seyfarth, 2008), thereby preventing the stance knee from excessively bending. Beyond the control of running, this method of creating a virtual compliant element was instrumental in maintaining good ground contact forces for large step-down walking experiments (see (Park et al., 2011) for

5 inches step-down, and (Park et al., 2012) for up to 8 inches step-down.) Furthermore, as will be seen in Section IV-F, virtual compliance can easily account for cable stretch and for asymmetry of the robot due to the boom, that are not included in the model for control.

C. Discrete-time Control

1) Hybrid Invariance: The controller (10) renders the zero dynamics manifold forward invariant and attractive. However, at discrete transitions, there is no guarantee that the post-transition state may belong on the zero dynamics manifold of the subsequent phase. In particular, $x_{\mathrm{s}}^- \in Z_{\alpha_{\mathrm{s}}}$, $x_{\mathrm{f}}^- \in Z_{\alpha_{\mathrm{f}}}$ does not guarantee that, $x_{\mathrm{f}}^+ = \Delta_{\mathrm{s}\to\mathrm{f}}(x_{\mathrm{s}}^-) \in Z_{\alpha_{\mathrm{f}}}$, and $x_{\mathrm{s}}^+ = \Delta_{\mathrm{f}\to\mathrm{s}}(x_{\mathrm{f}}^-) \in Z_{\alpha_{\mathrm{s}}}$. To ensure that the zero dynamics is invariant under the transition mappings, i.e., hybrid invariant, we introduce correction polynomials as in (Chevallereau et al., 2009). This is achieved by modifying the virtual constraints at event transitions as follows,

$$\begin{aligned} y_c^p &:= h_p\left(q_p, \alpha_p, \alpha_c^p\right) \\ &= H_0^p q_p - h_d^p\left(\theta_p, \alpha_p\right) - h_c^p\left(\theta_p, \alpha_p^c\right), \end{aligned} \tag{15}$$

where, the output consists of the previous output (8), and an additional correction term h_c^p, which correspond to Bézier polynomials whose coefficients are selected so that the post transition output and its velocity are zero, i.e., $y_c^{p+} = 0, \dot{y}_c^{p+} = 0$. Under the assumption of hybrid invariance, the hybrid zero dynamics is well defined and it governs the existence and stability properties of periodic orbits that correspond to running motions of the higher-dimensional robot. The surface (11) will become $\mathcal{Z}_{\alpha_{\mathrm{s}},\alpha_{\mathrm{c}}^{\mathrm{s}}}$ under the modified output (15).

2) Exponential Stability: To ensure that the periodic running orbit of interest is locally exponentially stable as a solution of the lower-dimensional hybrid zero dynamics—hence, locally exponentially stable in the higher-dimensional robot—we introduce the controller Γ^β acting in discrete time to update certain parameters $\beta \in \mathcal{B}$, which includes various physically relevant quantities such as leg touchdown and torso liftoff angles; for details see Section IV-E. To design the controller, we employ the method of Poincaré as follows. A periodic orbit representing a running gait is sampled at a Poincaré section $\mathcal{S}_\beta$, to define a Poincaré map $P_\beta : \mathcal{S}_\beta \times \mathcal{B} \to \mathcal{S}_\beta$, which gives rise to a discrete-time nonlinear control system

$$x^-[k+1] = P_\beta\left(x^-[k], \beta[k]\right), \tag{16}$$

where the parameters β are inputs available for control. Linearizing (16) about the fixed-point $(x^{-*}, 0)$ corresponding to the periodic orbit results in

$$\begin{aligned} \delta x^-[k+1] = &\left.\frac{\partial P_\beta}{\partial x^-}\right|_{(x^{-*},0)} \delta x^-[k] + \\ &\left.\frac{\partial P_\beta}{\partial \beta}\right|_{(x^{-*},0)} \beta[k], \end{aligned} \tag{17}$$

where $\delta x^- = x^- - x^{-*}$. A discrete LQR is then used to update the parameters β according to

$$\beta[k] = \Gamma^\beta(\delta x^-[k]) := K_{LQR}\ \delta x^-[k]. \tag{18}$$

such that the eigenvalues of the closed-loop system are within the unit circle.

3) Robustness to Perturbations: The control constructions so far render the desired periodic running gaits locally exponentially stable. To enhance the robustness of our control design, an additional event-based controller is introduced to update a set of parameters $\gamma \in \mathcal{G}$, which includes parameters to modify the virtual compliance stiffness, and swing height. The nonlinear controller that is used to modify the γ parameters is detailed in Section IV-E. We only mention that the control design is motivated by insight obtained in the context of controlling simpler hopper models, such as the SLIP. Special attention is paid to ensure the exponential stability property is preserved under the action of the controller by studying the properties of the Poincaré map, $P_\gamma : \mathcal{S}_\gamma \times \mathcal{B} \times \mathcal{G} \to \mathcal{S}_\gamma$, that includes all four layers of control.

IV. Controller Implementation Details

A. Virtual Constraint Design for Stance

During stance, the objective of the controller is threefold. First, it ensures that the torso enters the flight phase with suitable initial conditions so that excessive torso pitching is avoided. Second, it guarantees sufficient ground clearance of the swing leg to allow its proper positioning in anticipation to touchdown. And third, it creates a virtual compliance element that effectively "tunes" the physical leg stiffness to offer enhanced control authority during the stance phase.

The first two objectives of the stance control action can be achieved by devoting three out of the four available actuators to impose virtual holonomic constraints on the torso motion captured by its pitch angle q_{Tor} and on the motion of the swing leg described by the angles $q_{\mathrm{LA_{sw}}}$ and $q_{\mathrm{mLS_{sw}}}$. Hence, in defining the output (8) for stance, we choose the controlled variables as

$$H_0^{\mathrm{s}} q_{\mathrm{s}} = \left(q_{\mathrm{LA_{sw}}},\quad q_{\mathrm{mLS_{sw}}},\quad q_{\mathrm{Tor}}\right)'. \tag{19}$$

The virtual constraints imposed on the control variables (19) are parametrized by 5$^{\text{th}}$ order Bézier polynomials through the monotonically increasing angle θ_{s} formed by the virtual leg connecting the toe with the hip relative to the ground,

$$\theta_{\mathrm{s}}\left(q_{\mathrm{s}}\right) = \pi - q_{\mathrm{LA_{st}}} - q_{\mathrm{Tor}}, \tag{20}$$

see Figure 2(a). The detailed design of the constraints is documented in (Sreenath, 2011, Sec. 6.3). We only mention here that substantial torso control can be developed only during stance, due to the fact that the angular momentum about the center of mass is conserved in the flight phase. To avoid excessive pitching motions during the ensuing flight phase, the corresponding virtual

holonomic constraint imposed on q_{Tor} is designed to drive the torso so that at the end of the stance phase it leans forward with a backward angular velocity. This is important because a forward torso velocity at the beginning of flight would result in an excessive forward pitch at the end of flight due to the conservation of angular momentum, requiring correction of a large torso error during the relatively short—compared to the walking motions in (Sreenath et al., 2011b)—stance phase. To realize an actively tuned virtual compliant component as described in Section III-B2, we make use of the fourth actuator $u_{\mathrm{mLS_{st}}}$, which is available for control.

The stance phase zero dynamics—namely the dynamics compatible with the virtual constraints imposed on the controlled variables (19)—obtains the form (13) as was described in Remark 1, where $u_{\mathrm{mLS_{st}}}$ is chosen according to the prescription (14) in Section III-B2, thereby completing the control design during stance.

B. Virtual Constraint Design for Flight

During flight, the controller serves two purposes. First, it rapidly lifts the stance leg[2] to avoid toe stubbing at the early stages of its swing phase. Second, it positions the swing leg, whose touchdown is anticipated, at a proper absolute angle. To achieve these objectives, all four actuators will be recruited to enforce suitable virtual holonomic constraints by zeroing the output functions (8), in which the controlled variables are chosen as

$$H_0^{\mathrm{f}} q_{\mathrm{f}} = \left(q_{\mathrm{mLS_{st}}}, \quad q_{\mathrm{LA_{sw}}} + q_{\mathrm{Tor}}, \quad q_{\mathrm{mLS_{sw}}}, \quad q_{\mathrm{LA_{st}}}\right)', \tag{21}$$

where $(q_{\mathrm{mLS_{st}}}, q_{\mathrm{LA_{st}}})$ refer to the coordinates of the stance leg (the leg that was in stance and switched to swing for the flight phase.) Similarly to the stance phase, 5th order Bézier polynomials are employed to design the virtual holonomic constraints. The polynomials are parametrized based on the monotonically increasing quantity θ_{f}, which corresponds to the horizontal position of the hip,

$$\theta_{\mathrm{f}}\left(q_{\mathrm{f}}\right) = p^h_{\mathrm{hip}}. \tag{22}$$

C. Event Transitions

Transitions between continuous-time phases offer the possibility of updating certain parameters that are introduced through the virtual constraints—e.g., Bézier polynomial coefficients—to achieve the control objectives, such as the hybrid invariance condition described in Section III-C1. Up to this point, we have considered two transitions, which are imposed by the physics of the robot running; namely, the stance-to-flight and the flight-to-stance transitions occurring at the switching surfaces $\mathcal{S}_{\mathrm{s}\to\mathrm{f}}, \mathcal{S}_{\mathrm{f}\to\mathrm{s}}$ and governed by the transition maps $\Delta_{\mathrm{s}\to\mathrm{f}}, \Delta_{\mathrm{f}\to\mathrm{s}}$, respectively; see Section II for definitions.

[2]During flight both feet are off the ground, however we continue to use stance leg to mean the leg that was on the ground during the stance phase and similarly for the swing leg.

In addition to the transitions separating the stance and flight phases, we will further divide stance into two subphases: the stance-compression (sc) and the stance-decompression (sd). The transition from stance-compression to stance-decompression occurs at the switching surface

$$\mathcal{S}_{sc\to sd} = \left\{x_{\mathrm{s}} \in TQ_{\mathrm{s}} \mid H_{sc\to sd}\left(x_{\mathrm{s}}\right) = 0\right\}, \tag{23}$$

where the threshold function is $H_{sc\to sd} := \theta_{\mathrm{s}} - \theta_{sd}$, with θ_{s} defined by (20) and θ_{sd} a constant. The corresponding transition map is the identity map, i.e., $\Delta_{sc\to sd} := \mathrm{i}d$, reflecting the fact that the state does not change as the robot passes from stance compression to decompression.

In contrast to the state that remains unchanged through $\mathcal{S}_{sc\to sd}$, certain parameters characterizing the stance subphases can be updated as the controller switches from compression to decompression. In particular, the stiffness and rest position, $\alpha_{\mathrm{vc}} = (k_{\mathrm{vc}}, q_{\mathrm{mLS_{vc}}})$, of the virtual compliant element (14) introduced through the stance-phase continuous control action of Section III-B2 can have different values during the two stance subphases. Hence, in the stance-compression and stance-decompression phases, α_{vc} will be chosen as $\alpha^{sc}_{\mathrm{vc}}$ and $\alpha^{sd}_{\mathrm{vc}}$, respectively, with $\alpha^{sc}_{\mathrm{vc}} \neq \alpha^{sd}_{\mathrm{vc}}$. The update ensures that the parameters are only changed at transitions, i.e., $\dot{\alpha}_{\mathrm{vc}} = 0$ for the continuous dynamics. Intuitively, this parameter update facilitates energy injection during the stance-decompression to enable lift-off.

D. Gait Design Through Optimization

A periodic running gait is designed through an optimization procedure that selects the parameters introduced by the virtual constraints and the virtual compliance element to minimize energy consumption per step, subject to constraints to meet periodicity as well as workspace and actuator limitations. In more detail, the cost function employed is

$$J_{nom}\left(\alpha_{\mathrm{s}}, \alpha_{\mathrm{f}}, \alpha^{sc}_{\mathrm{vc}}, \alpha^{sd}_{\mathrm{vc}}\right) = \frac{1}{p^h_{\mathrm{toe_{sw}}}\left(q^-_{\mathrm{f}}\right)} \int_0^{T_I} ||u(t)||^2 dt, \tag{24}$$

where T_I is the step duration (stance plus flight time) and $p^h_{\mathrm{toe_{sw}}}$ is the step length. Minimizing this cost function tends to reduce peak torque demands and minimize the electrical energy consumed per step. The nonlinear constrained optimization routine `fmincon` of MATLAB's Optimization Toolbox is used to perform the numerical search for desired gaits, optimizing 31 different parameters; further details can be found in (Sreenath, 2011).

Following this procedure, a nominal periodic running gait at 1.34 m/s is obtained. Figure 4 depicts the virtual constraints for the stance and flight phases, along with other configuration variables, during one step of running. The squares on the plots indicate the transition from stance to flight phase. The step duration is 525 ms with 69% spent in stance and 31% in flight. On entry into the flight phase, the torso is leaning forward (negative torso angle) and is rotating backward (positive torso velocity).

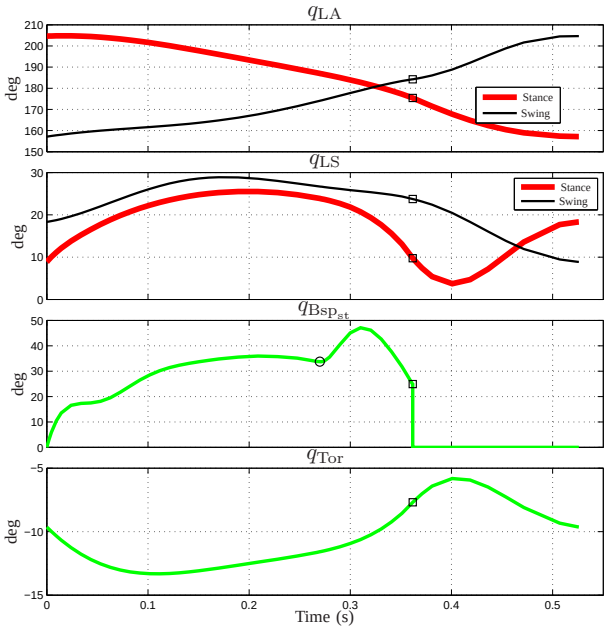

Fig. 4. Evolution of the virtual constraints and configuration variables for a nominal fixed point (periodic running gait) at a speed of 1.34 m/s and step length 0.7055 m. The squares illustrate the location of transition between stance to flight phase. The circle on the $q_{\mathrm{Bsp_{st}}}$ plot illustrates the location of the *sc* to *sd* event transition.

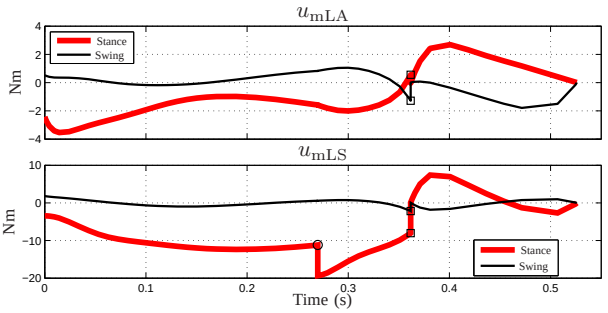

Fig. 5. Actuator torques corresponding to the nominal fixed point. The squares illustrate the location of transition between stance to flight phase. The circle on the $u\mathrm{mLS_{st}}$ plot illustrates the location of the *sc* to *sd* event transition. Note that the torques are discontinuous at stance to flight transitions. Also note the additional discontinuity for $u\mathrm{mLS_{st}}$ at the *sc* to *sd* event transition due to the instantaneous change in the offset for the virtual compliance at this transition.

The swing leg angle travels roughly 57% of its total 47.5° during the stance phase[3] and needs to travel the remaining 43% in the flight phase which is of smaller duration. Thus the velocities of the joints in the flight are high compared to those of the stance phase.

Figure 4 also illustrates the evolution of the leg shape and the stance $\mathrm{B_{spring}}$ variables. During the stance-compression phase the spring compresses, reaches its peak value of almost 36° and starts to decompress. On transition to stance-decompression, the motor injects energy into the system causing the spring to rapidly compress to a peak of 47°. At lift-off, when the vertical component of the ground reaction force goes to zero, the spring is compressed to approximately 25°. At the early stages of the ensuing flight phase, the stance leg (the leg that was in stance and switched to swing) unfolds due to the large velocity at push-off, as the spring rapidly decompresses.

Figure 5 illustrates the actuator torques used to realize the gait, and all motor torques are well within the capacity of the actuators, namely 30 Nm. The stance leg shape torque is relatively large, initially to support the weight of the robot as the stance knee bends, and subsequently to inject energy in the stance-decompression phase to achieve lift-off. Note that the stance motor leg shape torque is discontinuous at the stance-compression to stance-decompression transition due to an instantaneous change in the parameters α_{vc} of the virtual compliance. All torques are discontinuous at the stance-to-flight transition due to the impact of the spring with the hard-stop; see Figure 2(b).

Figure 6 illustrates the evolution of the swing leg height and the vertical position of the center of mass of the robot. The swing foot is over 15 cm above the ground at its peak to offer good ground clearance for hard impacts. During the stance phase, the COM undergoes an asymmetric motion with the lowest point of potential energy being around 52% into the stance phase. During the flight phase, the COM has a ballistic trajectory. As noted in (McMahon and Cheng, 1990) and (Holmes et al., 2006), both these aspects of COM motion are dominant characteristics of running. Finally, Figure 7 illustrates the vertical component of the ground reaction force. Immediately upon impact, during the stance-compression phase, there is a peak in the ground reaction force due to the spring compressing rapidly on impact. During most of the stance-compression phase, the force is fairly constant. On transition to stance-decompression phase, the energy injection causes the force to rapidly first increase and then go to zero at which point stance to flight transition occurs.

E. Parameter Update Strategies

1) Exponential Stability: To analyze the stability of the running gait obtained in Section IV-D in closed loop with the continuous-time controllers (12), we employ the method of Poincaré. Let $\mathcal{S}_{sc\to sd}$ be the Poincaré section. Then, the stability properties of the periodic running orbit can be captured by the stability properties of the corresponding fixed point of the restricted Poincaré map $\rho : \mathcal{S}_{sc\to sd} \cap \mathcal{Z}_{\alpha_{\mathrm{s}},\alpha_c^{\mathrm{s}}} \to \mathcal{S}_{sc\to sd} \cap \mathcal{Z}_{\alpha_{\mathrm{s}},\alpha_c^{\mathrm{s}}}$; see (Morris and Grizzle, 2005, 2009). Numerical computations of the eigenvalues of the linearization of the restricted Poincaré map about the fixed point of interest reveals that the corresponding running gait is unstable with a dominant

[3]Contrast this to that of humans, where the legs travel rougly 90% of the range of travel during the stance phase.

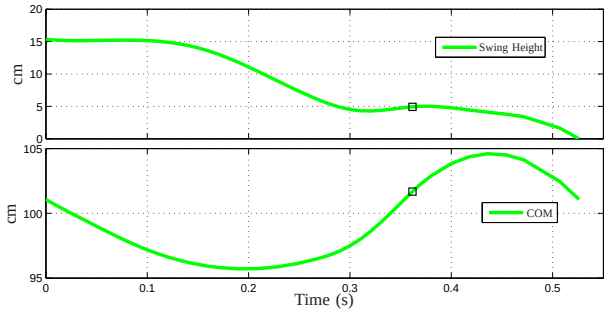

Fig. 6. Evolution of swing leg height and vertical center of mass (COM) of the robot for the nominal fixed point. The COM trajectory clearly illustrates the lowest point of potential energy during the stance phase and the ballistic trajectory in the flight phase, both of which are dominating characteristics of running. The squares illustrate the location of transition between stance to flight phase.

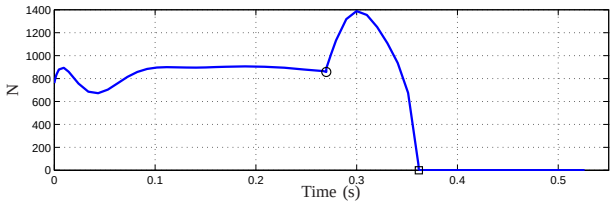

Fig. 7. Vertical component of the ground reaction force for the nominal running fixed point. At the *sc* to *sd* event transition (indicated by the circle), the change in the offset for the virtual compliance causes the spring to compress further which increases the ground reaction force considerably. Takeoff occurs when the ground reaction force goes to zero (indicated by the square.)

eigenvalue of magnitude 1.19. In fact, all the running gaits we have been able to compute were unstable.

To locally exponentially stabilize the desired running gait, we introduce the additional outer-loop discrete-time controller Γ^β. These parameters are a subset of those introduced through the continuous-time control action—namely, $\alpha_{\rm s}, \alpha_{\rm f}, \alpha^{sc}_{\rm vc}, \alpha^{sd}_{\rm vc}$—and are denoted by β to emphasize the fact that they are updated via the loop Γ^β of Figure 3 to ensure stability. The parameters β include the stiffness and rest position of the virtual compliant element (14), which enables modifying the energy stored during compression and injected during decompression; $\beta^p_{k_{\rm vc}}, \beta^p_{q_{\rm mLS_{vc}}}$ for $p \in \{sc, sd\}$. In addition, they include the touchdown angle β_{TD} of the swing leg to regulate the forward running speed, the torso angle at liftoff $\beta_{\rm Tor}$ that influences the initial conditions of the ensuing flight phase, and an offset $\beta_{\theta_{\rm f}}$ that is added to $\theta^-_{\rm f}$ to change the position of liftoff. In summary,

$$\beta = (\beta^{sc}_{k_{\rm vc}}, \beta^{sd}_{k_{\rm vc}}, \beta_{TD}, \beta^{sc}_{q_{\rm mLS_{vc}}}, \beta^{sd}_{q_{\rm mLS_{vc}}}, \beta_{\theta_{\rm f}}, \beta_{\rm Tor}) \in \mathcal{B}$$

includes the parameters that are updated in an event-based fashion by the component Γ^β of the control law.

For the design and experimental implementation of Γ^β, the full-order Poincaré map is considered. The switching surface in the definition of the Poincaré map P_β in Section III-C2 is chosen as $\mathcal{S}_\beta = \mathcal{S}_{sc\to sd}$, resulting in the discrete-time nonlinear control system (16) with β appearing as its input. The controller Γ^β corresponds to

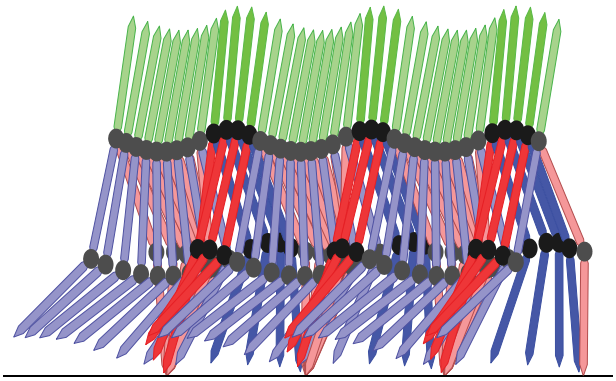

Fig. 8. Stick figure plot of three steps of running. The stance leg is illustrated in red, while the swing leg is illustrated in blue. Stick figures with darker shades are in flight phase, while those with lighter shades are in stance phase. From the stick figure it can be easily deduced that the flight phase lasts around 30% of the gait.

the discrete LQR (18) designed based on the linearization (17) of (16) about the fixed point (x^{-*}, β^*) as was discussed in Section III-C2. This controller updates β each time the surface $\mathcal{S}_{sc\to sd}$ is crossed, ensuring that the eigenvalues of linearization of the closed-loop Poincaré map are all within the unit circle; for the particular design implemented here, the dominant eigenvalue has magnitude 0.8383, concluding that the fixed point is locally exponentially stable.

Figure 8 shows three steps of the running gait under the controller that includes Γ^α_p, $\Gamma^{\alpha_c}_p$, and Γ^β. The obtained motion can continue indefinitely in simulation.

2) Robustness to Perturbations: The control design proposed so far combines continuous- and discrete-time control to exponentially stabilize the system, accommodating perturbations in the torso pitch angle up to 6° in both the forward and backward directions. While this performance in stabilizing the torso is adequate for experimental implementation, the controller in its current form cannot reject errors in the stance leg shape that exceed 5° at impact; see Figure 9(a). This observation motivates the additional control layer Γ^γ of Figure 3, which, as was mentioned in Section III-C3 is added to improve the robustness of our control design to perturbations in the knee angle at impact.

To implement this controller, a number of parameters detailed below will be updated by Γ^γ on entry to the stance phase; that is, at the switching surface $\mathcal{S}_\gamma = \Delta_{\rm f\to s}(\mathcal{S}_{\rm f\to s}) \subset TQ_{\rm s}$, where $\mathcal{S}_{\rm f\to s}$ is the flight-to-stance switching surface defined by (6) and $\Delta_{\rm f\to s}$ the corresponding transition map. The motivation for considering the touchdown event is that it provides an immediate response to errors arising in the preceding flight phase, such as landing with an excessively bent knee, or velocity mismatch caused by imperfections in the ground contact model.

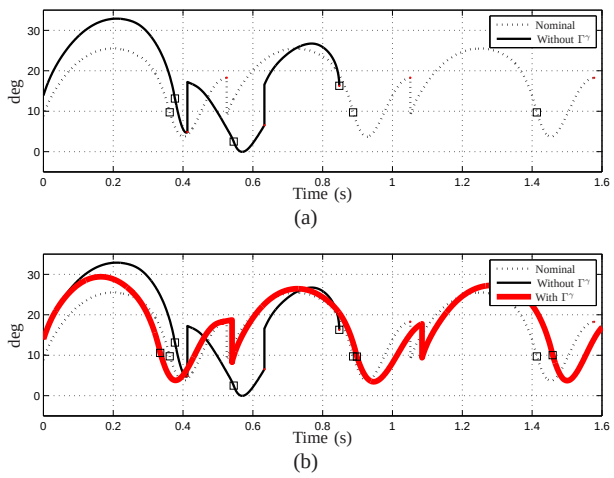

Fig. 9. Three step simulation of a 5° perturbation in the impact value of the leg shape. (a) Perturbation without Γ^γ outer-loop controller, (b) Perturbation with Γ^γ outer-loop controller. The nominal (no perturbation) plot is shown for comparision. The squares on the plots indicate locations at which the controller transitions from stance to flight phase.

We continue our discussion on this additional control component Γ^γ by providing some intuition. First note that, to produce the same leg force, the compression required in a segmented revolute-knee leg with joint compliance is larger than that required in a prismatic leg. This phenomenon was observed in (Rummel and Seyfarth, 2008), and, in the context of MABEL, implies that the stiffness of the virtual compliant element should be modified—i.e., increased—to prevent the leg from excessively bending to develop sufficient force for supporting the weight of the robot. Furthermore, the swing leg may have to contract additionally to ensure sufficient ground clearance in the presence of shorter stance leg lengths. To accommodate these requirements, the virtual compliance stiffness, $\gamma^{sc}_{k_{\rm vc}}$, as well as the knee angle of the swing leg $\gamma_{\rm LS_{sw}}$ will be updated according to

$$\gamma^{sc}_{k_{\rm vc}} = \begin{cases} K_{k^{sc}_{\rm vc}}(q^{s+}_{\rm LS_{st}} - q^{s+*}_{\rm LS_{st}}), & q^{s+}_{\rm LS_{st}} - q^{s+*}_{\rm LS_{st}} > 0 \\ 0, & \text{otherwise} \end{cases}$$
$$\gamma_{\rm LS_{sw}} = \begin{cases} K_{\rm LS_{sw}}(q^{s+}_{\rm LS_{st}} - q^{s+*}_{\rm LS_{st}}), & q^{s+}_{\rm LS_{st}} - q^{s+*}_{\rm LS_{st}} > 0 \\ 0, & \text{otherwise} \end{cases} \tag{25}$$

where $q^{s+}_{\rm LS_{st}}$ denotes the stance leg shape angle right after touchdown, $q^{s+*}_{\rm LS_{st}}$ its nominal value. The gains $K_{k^{sc}_{\rm vc}}, K_{\rm LS_{sw}}$ are tuned through simulations, and their values are provided in Table I.

An additional corrective action embedded in Γ^γ regards the regulation of the forward running speed. To do this, Γ^γ updates a parameter $\gamma_{\rm Tor}$, which shapes the virtual holonomic constraint imposed on the torso motion at the beginning of stance based on the difference between the current forward speed and its nominal value. This allows leaning the torso forward to increase speed, or backward to decrease speed, and is implemented

TABLE I
GAIN PARAMETERS FOR Γ^γ CONTROLLER.

Gain parameter	Value
$K_{k^{sc}_{\rm vc}}$	0.46
$K_{\rm LS_{sw}}$	1.5
$K^{+}_{\rm Tor}$	0.16
$K^{-}_{\rm Tor}$	0.31
$K_{\delta_{sc\to sd}}$	-0.37

through the prescription

$$\gamma_{\rm Tor} = \begin{cases} K^{+}_{\rm Tor}(\dot{p}^{h,s+}_{\rm hip} - \dot{p}^{h,s+*}_{\rm hip}), & (\dot{p}^{h,s+}_{\rm hip} - \dot{p}^{h,s+*}_{\rm hip}) > 0 \\ K^{-}_{\rm Tor}(\dot{p}^{h,s+}_{\rm hip} - \dot{p}^{h,s+*}_{\rm hip}), & \text{otherwise,} \end{cases} \tag{26}$$

where $\dot{p}^{h,s+}_{\rm hip}$ is the horizontal speed of the hip at impact with the ground, $\dot{p}^{h,s+*}_{\rm hip}$ its nominal value, and gains $K^{+}_{\rm Tor}, K^{-}_{\rm Tor}$ are provided in Table I. As speed increases, the energy injected during the stance-decompression phase decreases because the time spent in this phase decreases with increasing speed. To account for this, the controller Γ^γ will update one more parameter, namely $\gamma_{\delta_{sc\to sd}}$, that modifies the location of transition from stance-compression to stance-decompression to increase or decrease the period over which energy is injected in the stance-decompression phase. This is achieved through

$$\gamma_{\delta_{sc\to sd}} = \begin{cases} K_{\delta_{sc\to sd}}(\dot{p}^{h,s+}_{\rm hip} - \dot{p}^{h,s+*}_{\rm hip}), & (\dot{p}^{h,s+}_{\rm hip} - \dot{p}^{h,s+*}_{\rm hip}) > 0 \\ 0, & \text{otherwise} \end{cases} \tag{27}$$

where $\dot{p}^{h,s+}_{\rm hip}$ and $\dot{p}^{h,s+*}_{\rm hip}$ have the same meaning as in (26) and $K_{\delta_{sc\to sd}}$ is provided in Table I. In summary,

$$\gamma = (\gamma^{sc}_{k_{\rm vc}}, \gamma_{\rm Tor}, \gamma_{\rm LS_{sw}}, \gamma_{\delta_{sc\to sd}}) \in \mathcal{G}$$

includes the parameters that are updated in an event-based fashion by the component Γ^γ of the control law.

Under the influence of Γ^γ, the robustness to perturbations is increased and, as shown in Figure 9(b), perturbations up to 5° in the impact leg shape angle (knee being bent an additional 10°) can be rejected. The stability of the closed-loop system can be analyzed through the eigenvalues of the linearization of the Poincaré map P_γ introduced in Section III-C3; more details can be found in Appendix B where it is shown that the linearized Poincaré map has a dominant eigenvalue of magnitude 0.6072 indicating that the closed-loop system with the additional component Γ^γ is locally exponentially stable.

***Remark** 2:* Note that the controllers $\Gamma^\alpha, \Gamma^{\alpha_c}, \Gamma^\beta$ have been designed through rigorous control synthesis approaches, whereas the design of the outer most control loop, Γ^γ, has been based on heuristics. It is noted that the controllers $\Gamma^\alpha, \Gamma^{\alpha_c}, \Gamma^\beta$ achieve stable running in simulations on the design model. The controller Γ^γ aids in the experimental validation of running by increasing the closed-loop system's robustness to perturbations in the knee angle at impact and to imperfections in the ground contact model. Section V-D provides additional comments in this regard.

TABLE II
STIFFNESS CONSTANTS FOR VARIOUS SOURCES OF COMPLIANCE.

Source of compliance	Stiffness value
k_{Bsp}	3.17
k_{cable}	2.46
k^*_{vc}	1.66
k_{vc}	5.08

F. Preparing for Experimental Deployment

One aspect that needs to be incorporated in the control design prior to experimental deployment on MABEL is cable stretch. In the leg shape coordinates, cable stretch reaches a peak value of almost 15° just prior to lift-off, which, given that the nominal peak leg shape is around 25° (see Figure 4), amounts for over 60% of motion in the knee, thus further amplifying knee bending. To account for this issue, the nominal controller design will be modified. In more detail, the compliance due to cable stretch will be modeled as a spring-damper system placed in series with the physical spring ($\mathrm{B}_{\mathrm{spring}}$) and the motor leg shape actuator in the transmission mechanism. Then, active force control on the stance leg can be used to modify the virtual compliance k_{vc} so that the compliance due to the cable stretch k_{cable} together with k_{vc} has the value of the effective compliance k^*_{vc} obtained through the optimization procedure detailed in Section IV-D; i.e.,

$$\frac{1}{k_{cable}} + \frac{1}{k_{\mathrm{vc}}} = \frac{1}{k^*_{\mathrm{vc}}}. \tag{28}$$

With this modification, the effective compliance of the leg is now the same as that without cable stretch, i.e., cable stretch has been accounted for by the control design. Table II provides the values for the various compliances discussed in this section.

This modified running controller is next validated on the detailed model as mentioned in Section II-F and is ready for experimental deployment.

V. RUNNING EXPERIMENTS

This section documents experimental implementations of the running controller developed in Sections III, IV. To illustrate the power and limitations of the proposed method, three experiments are presented. The first experiment details the execution of a transition controller that transitions from walking to running, the second experiment details a running experiment, and finally the third experiment details the transition from running to walking. Videos of the running experiments are available on YouTube (Sreenath et al., 2011a,c).

A. Exp. 1: Two-step Transition from Walking to Running

Running on MABEL can be implemented by transitioning from walking. As in (Westervelt et al., 2003), to transition from walking to running the controller modifies the virtual constraints corresponding to a walking gait so that, by the end of a walking step, they are closer to the virtual constraints of the targeted running gait. Instead of a one-step transition from walking to running as was done in (Morris et al., 2006), a two-step transition is implemented to enable a smoother transition by preventing rapid torso motions on MABEL. This is especially important for gaits where the final and initial values of the torso virtual constraint differ significantly between the walking and running fixed points, respectively. A walking-to-running transition then consists of the following: (a) A transition from the nominal walking gait to a transition-walk-step, followed by (b) a transition from the transition-walk-step to a transition-run-step, and finally (c) a transition from the transition-run-step to the nominal running gait. Figure 10(a) illustrates plots of various variables for the transition from walking to running. The walking and running sections are clearly marked along with the two transition steps.

B. Exp. 2: Running with Point Feet

Initial experiments on MABEL failed to achieve steady-state running due to foot slippage and the controller's poor performance in regulating forward speed. This is a consequence of imperfections in the ground contact model used in the controller design. To address these issues, the point feet were replaced with passive feet with shoes to provide a larger surface area for traction, thereby preventing slipping. With this configuration, successful running was achieved—see Appendix A for more details on these experiments—suggesting certain modifications to the running controller of Sections III, IV in order to achieve running on point feet.

In more detail, to regulate the forward speed, the γ-parameter corresponding to the virtual compliance is modified as in (31) and saturation in the β-parameter corresponding to the touchdown angle is introduced as in (32); see Appendix A. Finally, the γ-parameter that modifies the location of the stance-compression to stance-decompression phase will also be saturated as a function of the speed as,

$$\gamma^{sat}_{\delta_{sc\to sd}} = \begin{cases} 0.2, & 0 \le \dot{p}^{h,avg}_{\mathrm{hip}} < 2 \\ 0.25, & 2 \le \dot{p}^{h,avg}_{\mathrm{hip}} < 2.5 \\ 0.35, & 2.5 \le \dot{p}^{h,avg}_{\mathrm{hip}} \end{cases}. \tag{29}$$

At high speeds, the time spent in the stance-decompression phase decreases, which results in less energy being injected and smaller push-offs. With the above modification, a well defined flight phase is maintained even at fast running motions.

Next, to prevent the stance-decompression phase from causing a lift-off with a high velocity, the stance-decompression to flight phase switching surface is modified as follows

$$\mathcal{S}^{exp}_{sd\to \mathrm{f}} := \mathcal{S}_{sd\to \mathrm{f}} \cap \{x_{\mathrm{s}} \in TQ_{\mathrm{s}} \mid \dot{p}^{v}_{\mathrm{hip}} > \dot{p}^{v,s-*}_{\mathrm{hip}}\}. \tag{30}$$

In addition, during the stance-decompression phase, the torso is pushed back in a similar manner as in the running with feet experiment. Finally, during the flight phase, the

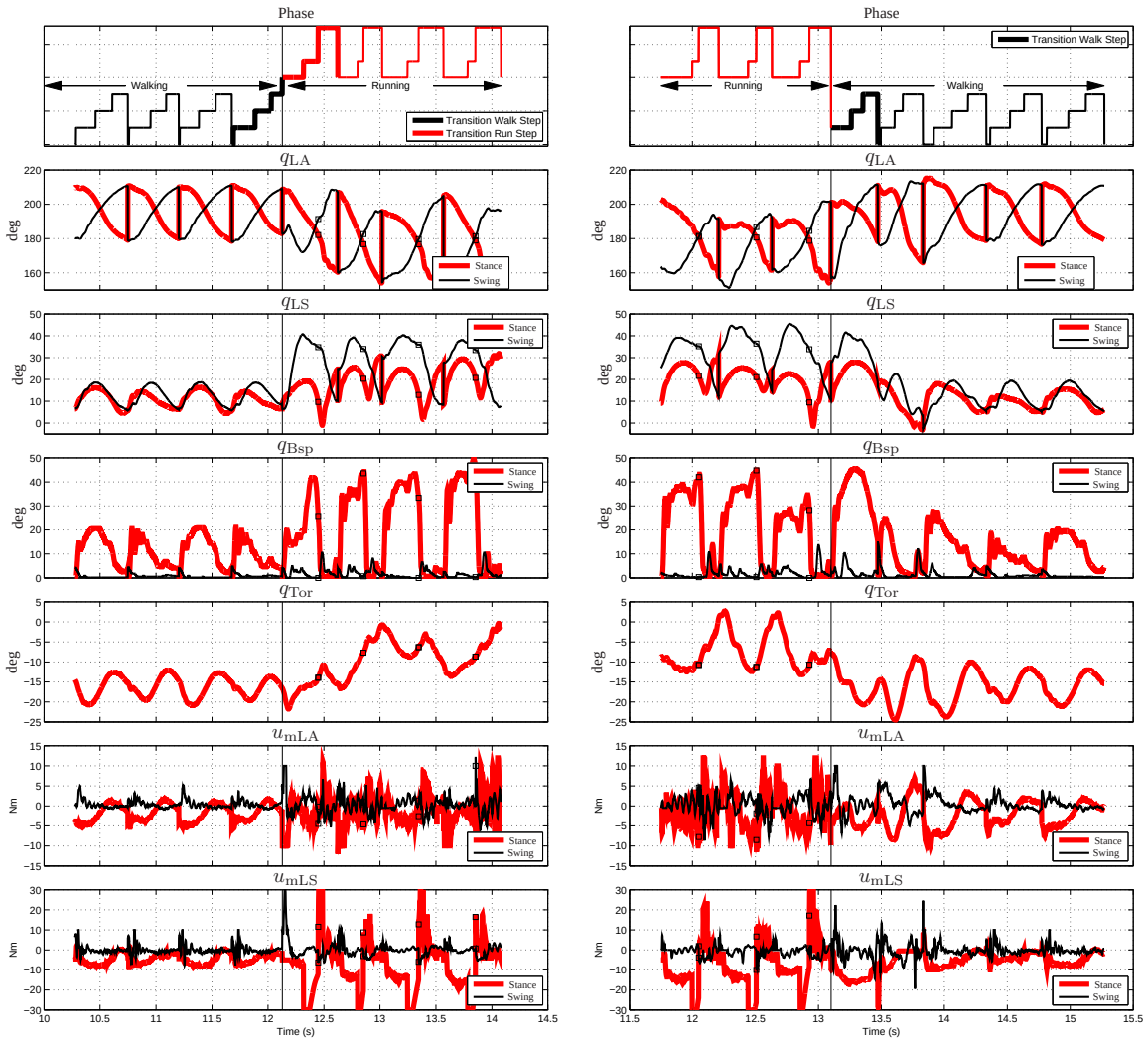

Fig. 10. Experimental plots of the internal phase variable, joint angles, and motor torques for (a) transition from walking to running (Exp. 1) and (b) transition from running to walking (Exp. 3). The internal phase variable of the controller indicates the walking and running parts of the gait, with the thicker plots indicating the transition steps. Note that, for transition to running there are two transition steps - one during walking and the other during running, while for transition to walking there is one transition step during walking. Also note that the peak spring compression for running is around 2.5 times that for walking.

adaptive correction polynomials, as used for the running with feet experiment, are deployed. Both these changes counteract the effect of unmodeled cable stretch in the leg angle direction.

With these changes to the controller developed in Sections III, IV, the running experiment is carried out as follows. First, walking is initiated on MABEL using the walking controller developed in (Sreenath et al., 2011b). Next, the walking to running transition controller, presented in Section V-A, is executed. Finally, on transition to running, the running controller is executed. The running controller induced stable running at an average speed of 1.95 m/s, and a peak speed of 3.06 m/s. 113 running steps were obtained and the experiment terminated when the power to the robot was cut off. At 2 m/s, the average stance and flight times of 233 ms and 126 ms are obtained respectively, corresponding to a flight phase that is 35% of the gait. At 3 m/s, the average stance and flight times of 195 ms and 123 ms are obtained respectively, corresponding to a flight phase that is 39% of the gait. An estimated ground clearance of $3-4$ inches ($7.5-10$ cm) is obtained. The specific cost of mechanical transport (c_{mt}), defined in (Collins and Ruina, 2005), was computed to be 1.07.

Figure 11(a) depicts snapshots at 100 ms intervals of a typical running step. Figure 12(a) depicts the mean joint angles, and motor torques temporally normalized over time, for 50 consecutive steps of running.

The outer-loop event based controller parameters are depicted in Figures 13(a), 14(a). Considerable variation in the speed is observed. In particular, when the speed exceeds 2.5 m/s, large changes in the touch down angle, β_{TD}, and the γ-parameter that affects the transition from stance-compression to stance-decompression,

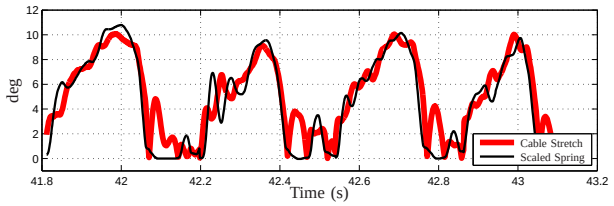

Fig. 15. Absolute value of leg shape cable stretch and spring compression for the stance leg for the running with point feet (Exp. 2.). Both variables are scaled to be in the leg shape coordinates. As is seen, cable stretch contributes as much as the spring to the compliance present in the system. This was hinted at in Table II.

$\gamma_{\delta_{sc\to sd}}$ causes the speed to dramatically drop to under 1 m/s. All this is autonomously handled by the controller with no manual intervention. The ability of the controller to recover from slow speeds below 1 m/s, and high speeds above 2.5 m/s illustrates a good robustness to imperfections in the ground contact model. The controller is also able to account for significant cable stretch (shown in Figure 15.)

C. Exp. 3: One-step Transition from Running to Walking

This section briefly describes the controller used to transition from running to walking. To realize such transitions, the running controller is switched to a walking controller that creates virtual compliance through active force control on the stance leg shape motor. This walking controller essentially treats a running-to-walking transition as a large step-down, similarly to what was done in (Park et al., 2012) for walking gaits. Figure 10(b) illustrates plots of various variables for the transition from running to walking. The running and walking sections are clearly marked along with the transition step. Note that transition from running to walking is achieved in a single step.

D. Discussion of the Experiments

The experimental implementation of running motions on MABEL revealed a number of interesting observations regarding the robot and the proposed controller. First, it was observed that the robot runs faster in experiments than what simulations predict based on the developed models. This behavior is similar to what was observed in walking experiments with MABEL (Sreenath et al., 2011b), and is attributed to the inevitable inaccuracies associated with the ground contact model. While in (Sreenath et al., 2011b, Sec. VII-B) we suggest various ways of modeling the ground impact demonstrating that impact scaling can account for speed differences in walking, it is not clear how the parameters of the compliant ground model can be selected to improve the accuracy of the simulations in the case of running.

Another source of inaccuracy is the assumption of planar motion that underlies the model based on which the controller is derived. Clearly, the support boom in the experimental setup constraints the robot's hip to move on the surface of a sphere and not in sagittal plane. Furthermore, the boom affects the weight distribution so that the robot weighs 10%—approximately 7 Kg—more when supported on the inner leg than when supported on the outer leg. In running, this asymmetry results in harder impacts on the inside leg causing its knee to bend more during the corresponding stance phase. As a consequence, the outer-loop component of the controller tends to overcompensate in the following step; notice the pronounced step-to-step oscillations in the virtual compliance in Figure 14(a). To account for this phenomenon, the controller can be modified so that the virtual compliance is 10% stiffer on the inside leg. Moreover, for smoother running motions, the outer-loop controllers can perform separate step-to-step updates over two steps.

As a final remark, note that the proposed controller combines formal control synthesis procedures with heuristics to experimentally realize running on MABEL. The inner-loop control components—namely, Γ^{α}, Γ^{α_c}, and Γ^{β}—are designed through systematic control methods to meet certain specifications such as hybrid invariance and local exponential stability. On the contrary, the outer-loop event-based controller Γ^{γ} is based on certain intuitive observations aiming to enhance the robustness of the controller to perturbations in the knee angle at impact and to imperfections in the ground contact model. To minimize the reliance of the controller on heuristics, the softening effect of the spring for large knee angles can be incorporated in the continuous-time control component by suitably modifying the virtual compliance (14) to include the nonlinear relation between the knee bending angle and the developed leg force as observed in (Rummel and Seyfarth, 2008). Similarly the effect of cable stretch can also be included in (14). With these modifications, the outer-loop components Γ^{γ} could be removed from the design and Γ^{β} would be sufficient to ensuring both exponential stability and robustness.

VI. Conclusion

MABEL contains springs in its drivetrain for the purposes of enhancing agility and robustness of dynamic locomotion. This paper has presented a model-based control design method to realize the potential of the springs. Experiments have been performed to illustrate and confirm important aspects of the feedback design.

The controller is based on the hybrid zero dynamics introduced in (Poulakakis and Grizzle, 2009b) and further developed and deployed experimentally in (Sreenath et al., 2011b). An important modification was the deliberate inclusion of actuation in the zero dynamics during the stance phase of running, which enabled active force control of the stance knee. Specifically, a virtual compliant element was created to dynamically vary the effective leg compliance during stance. An outer-loop

(a) (b)

Fig. 11. Snapshots of a typical running step for (a) running with point feet, and (b) running with passive feet, are shown at intervals of 100 ms. The snapshots progress temporally from left to right and from top to bottom. Videos of the experiments are available on YouTube (Sreenath et al., 2011a,c).

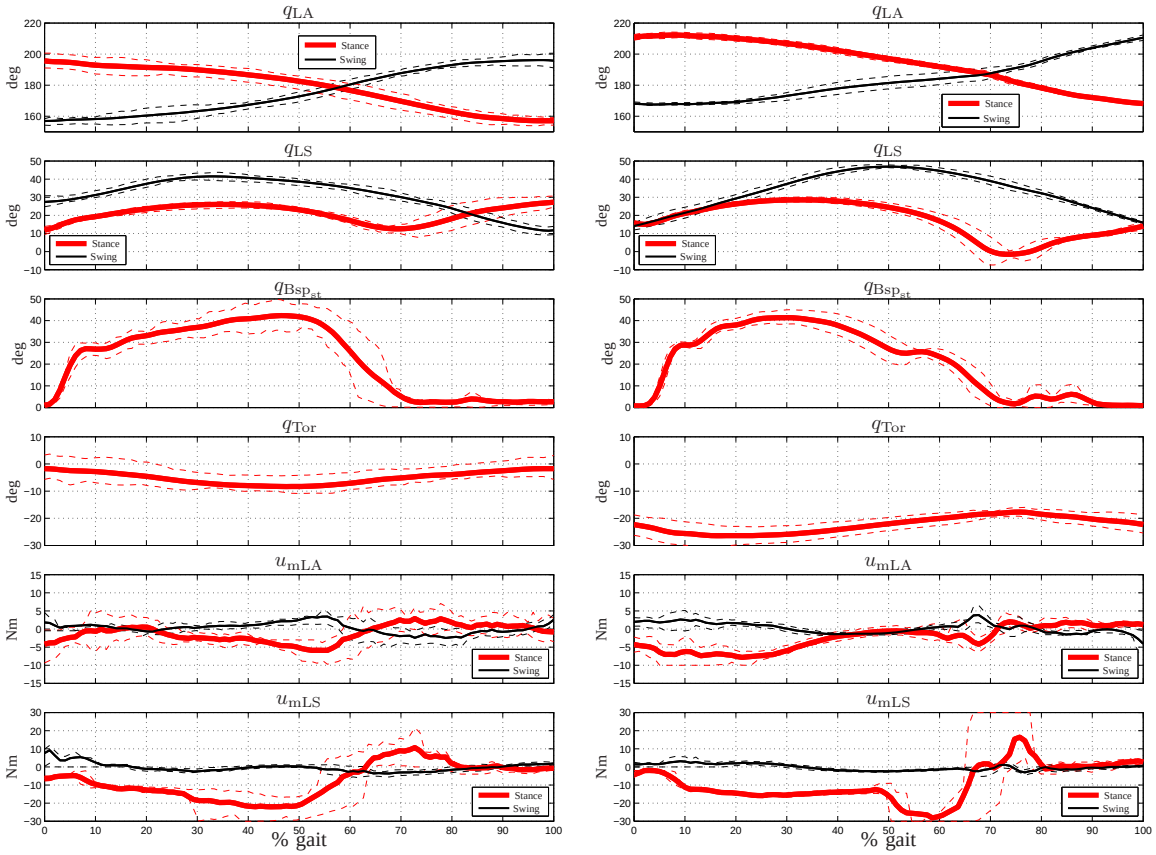

(a) (b)

Fig. 12. Ensemble plots of joint angles and motor torques of the stance and swing legs for 50 consecutive steps of (a) running with point feet, and (b) running with passive feet. The solid lines represent the mean recorded joint angle waveforms, while the dotted lines indicate the upper and lower quartiles over the running steps. The curves were temporally normalized from initial touchdown (0%) to subsequent touchdown (100%).

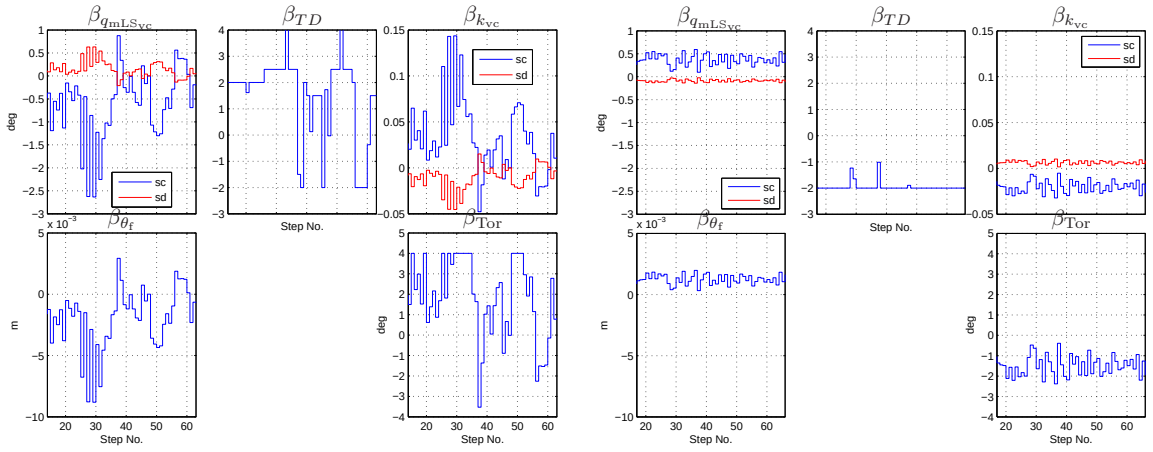

Fig. 13. Parameter plots for 50 consecutive steps for the outer-loop event-based controller, Γ^{β}, for (a) running with point feet and (b) running with passive feet. sc, sd refer to the values of the corresponding β-parameters in the stance-compression and stance-decompression subphases respectively.

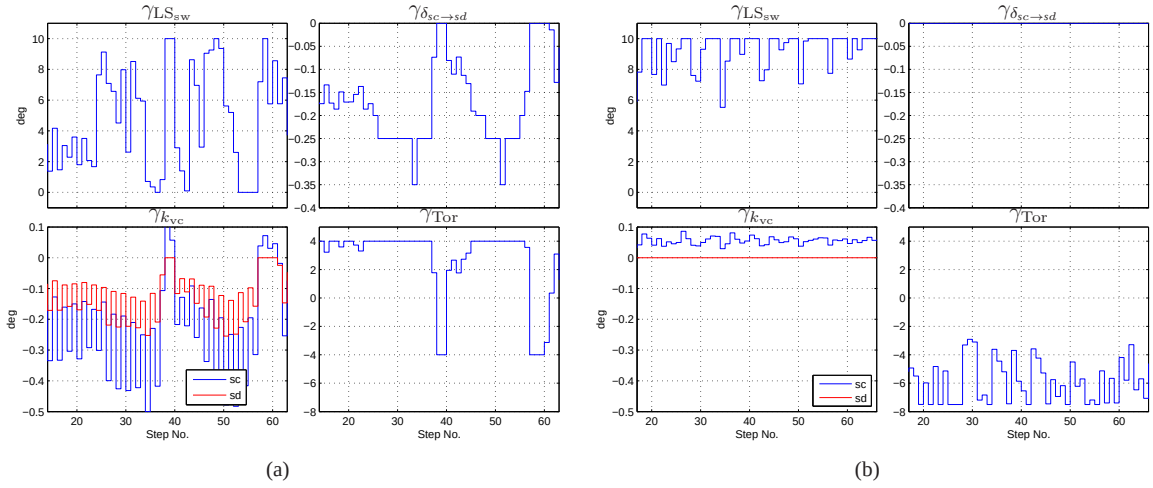

Fig. 14. Parameter plots for 50 consecutive steps for the nonlinear outer-loop controller for increasing robustness to perturbations , Γ^{γ}, for (a) running with point feet and (b) running with passive feet. sc, sd refer to the values of the corresponding γ-parameters in the stance-compression and stance-decompression subphases respectively.

event-based controller was designed to exponentially stabilize the periodic running gait. An additional outer-loop event-based controller was designed to improve the robustness of the periodic running gait to perturbations in the knee angle at impact and to imperfections in the ground contact model.

The running controller has been experimentally deployed and stable running has been successfully demonstrated on MABEL, both with passive feet and with point feet. The achieved running is dynamic and life-like, exhibiting flight phases of significant duration and high ground clearance. For running with point feet, the developed controller resulted in a kneed-biped running record of 3.06 m/s (10.9 kph or 6.8 mph).

Acknowledgments

The authors are grateful to A. Ramezani for his expert help with the experiments. K. Sreenath acknowledges L. McCauley for suggesting the experiments with nontrivial feet, and B. Morris is thanked for his advice - "Go big, or go home," which helped us to focus on multiple steps of running, and for his contributions to the theoretical underpinnings of our work, as cited in the text. J. Konscol is thanked for his weekly visits to the lab and for sharing his engineering experience, which contributed invaluably to the robustness of the electronic setup of the testbed. G. Buche is thanked for his many contributions to the design of the electronics, power supply, and safety interlock systems. Last but not least, we are deeply indebted to J. Hurst for designing MABEL. We hope that this paper has once again confirmed many of his expectations for the robot.

References

Ahmadi, M. and Buehler, M. (1997). Stable Control of a Simulated One-Legged Running Robot with Hip and Leg Compliance. 13(1):96–104.

Ahmadi, M. and Buehler, M. (2006). Controlled passive dynamic running experiments with the arl-monopod ii. *IEEE Transactions on Robotics*, 22(5):974–986.

Alexander, R. (1990). Three uses for springs in legged locomotion. *The International Journal of Robotics Research*, 9(2):53–61.

Ames, A. D., Gregg, R. D., Wendel, E. D. B., and Sastry, S. (2006). Towards the geometric reduction of controlled three-dimensional bipedal robotic walkers. In *3rd Workshop on Lagrangian and Hamiltonian Methods for Nonlinear Control*, pages 183–196.

Andrews, B., Miller, B., Schmitt, J., and Clark, J. E. (2011). Running over unknown rough terrain with a one-legged planar robot. *Bioinspiration & Biomimetics*, 6(2):1–15.

Chevallereau, C., Abba, G., Aoustin, Y., Plestan, F., Westervelt, E. R., de Wit, C. C., and Grizzle, J. W. (2003). Rabbit: a testbed for advanced control theory. *IEEE Control Systems Magazine*, 23(5):57–79.

Chevallereau, C., Grizzle, J. W., and Shih, C.-L. (2009). Asymptotically stable walking of a five-link underactuated 3d bipedal robot. *IEEE Transactions on Robotics*, 25(1):37–50.

Cho, B.-K., Park, S.-S., and ho Oh, J. (2009). Controllers for running in the humanoid robot, HUBO. In *IEEE-RAS International Conference on Humanoid Robots*, pages 385–390, Paris, France.

Collins, S. H. and Ruina, A. (2005). A bipedal walking robot with efficient and human-like gait. In *IEEE International Conference on Robotics and Automation*, pages 1983–1988, Barcelona, Spain.

Daley, M. A. and Biewener, A. A. (2006). Running over rough terrain reveals limb control for intrinsic stability. *Proceedings of the National Academy of Sciences of the United States of America*, 103(42):15681–15686.

Daley, M. A., Usherwood, J. R., Felix, G., and Biewener, A. A. (2006). Running over rough terrain: guinea fowl maintain dynamic stability despite a large unexpected change in substrate height. *The Journal of Experimental Biology*, 209:171–187.

Ferris, D. P. and Farley, C. T. (1997). Interaction of leg stiffness and surface stiffness during human hopping. *Journal of applied physiology*, 82:15–22.

Ferris, D. P., Louie, M., and Farley, C. T. (1998). Running in the real world: adjusting stiffness for different surfaces. *Proceedings of The Royal Society*, 265(1400):989–994.

Ghigliazza, R. M., Altendorfer, R., Holmes, P., and Koditschek, D. E. (2003). A Simply Stabilized Running Model. *SIAM Journal of Applied Dynamical Systems*, 2(2):187–218.

Gregg, R. D. and Spong, M. W. (2010). Reduction-based control of three-dimensional bipedal walking robots. *The International Journal of Robotics Research*, 29(6):680–702.

Grizzle, J. W., Hurst, J., Morris, B., Park, H.-W., and Sreenath, K. (2009). MABEL, a new robotic bipedal walker and runner. In *American Control Conference*, pages 2030–2036, Saint Louis, MO, USA.

Hirose, M. and Ogawa, K. (2007). Honda humanoid robots development. *Philosophical Transactions of The Royal Society A*, 365(1850):11–19.

Holmes, P., Full, R. J., Koditschek, D., and Guckenheimer, J. (2006). The dynamics of legged locomotion: Models, analyses, and challenges. *SIAM Review*, 48(2):207–304.

Hürmüzlü, Y. and Chang, T. (1992). Rigid body collisions of a special class of planar kinematic chains. *IEEE Transactions on Systems, Man and Cybernetics*, 22(5):964–71.

Hurst, J. W. (2008). *The Role and Implementation of Compliance in Legged Locomotion*. PhD thesis, Carnegie Mellon University.

Hurst, J. W. and Rizzi, A. A. (2008). Series compliance for an efficient running gait. *IEEE Robotics & Automation Magazine*, 15(3):42–51.

Isidori, A. (1995). *Nonlinear Control Systems*. Springer-Verlag, Berlin, third edition.

Kajita, S., Kaneko, K., and Morisawa, M. (2007). Zmp-based biped running enhanced by toe springs. In *IEEE International Conference on Robotics and Automation*, pages 3963–3969, Roma, Italy.

Kajita, S., Nagasaki, T., Kaneko, K., Yokoi, K., and Tanie, K. (2005). A running controller of humanoid biped hrp-2lr. In *IEEE International Conference on Robotics and Automation*, pages 616–622, Barcelona, Spain.

Koechling, J. C. (1989). *The limits of running speed: Experiments with a legged robot*. PhD thesis, Carnegie Mellon University, Pittsburgh, PA.

Koepl, D., Kemper, K., and Hurst, J. (2010). Force control for spring-mass walking and running. In *IEEE/ASME International Conference on Advanced Intelligent Mechatronics*, pages 639–644, Montreal, Canada.

McGeer, T. (1990). Passive bipedal running. *Proceedings of the Royal Society of London*, 240(1297):107–34.

McMahon, T. A. and Cheng, G. C. (1990). The mechanics of running: How does stiffness couple with speed? *Journal of Biomechanics*, 23(1):65–78.

McMahon, T. A., Valiant, G., and Frederick, E. C. (1987). Groucho running. *Journal of Applied Physiology*, 62(6):2326–37.

Morris, B. and Grizzle, J. W. (2005). A restricted Poincaré map for determining exponentially stable periodic orbits in systems with impulse effects: Application to bipedal robots. In *IEEE Conference on Decision and Control*, pages 4199–206, Seville, Spain.

Morris, B. J. and Grizzle, J. W. (2009). Hybrid invariant manifolds in systems with impulse effects with application to periodic locomotion in bipedal robots. *IEEE Transactions on Automatic Control*, 54(8):1751 – 1764.

Morris, B. J., Westervelt, E. R., Chevallereau, C., Buche, G., and Grizzle, J. W. (2006). *Achieving Bipedal Running with RABBIT: Six Steps Toward Infinity*,

volume 340 of *Lecture Notes in Control and Information Sciences*, pages 277–297. Springer Berlin / Heidelberg.

Nagasaka, K., Kuroki, Y., Itoh, S., and Yamaguchci, J. (2004). Integrated motion control for walking, jumping and running on a small bipedal entertainment robot. In *IEEE International Conference on Robotics and Automation*, pages 3189–3194, New Orleans, LA.

Park, H.-W., Sreenath, K., Hurst, J. W., and Grizzle, J. W. (2011). Identification of a bipedal robot with a compliant drivetrain: Parameter estimation for control design. *Control Systems Magazine*, 31(2):63–88.

Park, H.-W., Sreenath, K., Ramezani, A., and Grizzle, J. W. (submitted, 2012). Switching control design for accommodating large step-down disturbances in bipedal robot walking. In *IEEE International Conference on Robotics and Automation*.

Poulakakis, I. (2008). *Stabilizing Monopedal Robot Running: Reduction-by-Feedback and Compliant Hybrid Zero Dynamics*. PhD thesis, The University of Michigan.

Poulakakis, I. and Grizzle, J. W. (2009a). Modeling and control of the monopedal robot thumper. In *IEEE International Conference on Robotics and Automation*, pages 3327–3334, Kobe, Japan.

Poulakakis, I. and Grizzle, J. W. (2009b). The spring loaded inverted pendulum as the hybrid zero dynamics of an asymmetric hopper. *IEEE Transactions on Automatic Control*, 54(8):1779–1793.

Raibert, M. H. (1986). *Legged Robots that Balance*. MIT Press, Cambridge, MA.

Rummel, J. and Seyfarth, A. (2008). Stable running with segmented legs. *The International Journal of Robotics Research*, 27(8):919–934.

Sayyad, A., Seth, B., and Seshu, P. (2007). Single-legged Hopping Robotics Research. *Robotica*, 25:587–613.

Spong, M. W. (1999). Passivity based control of the compass gait biped. In *IFAC World Congress*.

Sreenath, K. (2011). *Feedback Control of a Bipedal Walker and Runner with Compliance*. PhD thesis, The University of Michigan, Ann Arbor, MI.

Sreenath, K., Park, H.-W., and Grizzle, J. W. (2011a). MABEL runs free! YouTube video.

Sreenath, K., Park, H.-W., Poulakakis, I., and Grizzle, J. W. (2011b). Compliant hybrid zero dynamics controller for achieving stable, efficient and fast bipedal walking on MABEL. *International Journal of Robotics Research*, 30(9):1170–1193.

Sreenath, K., Park, H.-W., Ramezani, A., and Grizzle, J. W. (2011c). MABEL runs in style. YouTube video.

Tajima, R., Honda, D., and Suga, K. (2009). Fast running experiments involving a humanoid robot. In *IEEE International Conference on Robotics and Automation*, pages 1571–1576, Kobe, Japan.

Westervelt, E. R., Grizzle, J. W., Chevallereau, C., Choi, J. H., and Morris, B. (2007). *Feedback Control of Dynamic Bipedal Robot Locomotion*. Taylor & Francis/CRC Press, Boca Raton, FL.

Westervelt, E. R., Grizzle, J. W., and de Wit, C. C. (2003). Switching and PI control of walking motions of planar biped walkers. *IEEE Transactions on Automatic Control*, 48(2):308–312.

APPENDIX A
RUNNING WITH PASSIVE FEET

To avoid slipping, MABEL's original shins terminating at point feet were replaced with shins terminating in passive feet enclosed in regular running shoes that provide a larger surface area for better traction. With the addition of the passive feet, the model developed in Section II is no longer valid due to (a) the different inertia properties between the two designs, and (b) the different toe-ground interactions, which, in the case of shoes, result in softer impacts due to the rolling contact with the ground. To accommodate these differences, a number of modifications will be made in the controller.

Modifications to regulate speed: At faster speeds, the time spent in the stance-decompression phase decreases. As a result, the effective energy injection is reduced, resulting in a lower peak apex height in flight. To maintain a well defined flight phase at fast speeds, an additional parameter, $\gamma_{\delta_{sc\to sd}}$ (see (27)), was added to Γ^{γ} to modify the location of the stance-compression to stance-decompression switching surface.

As suggested in (McGeer, 1990; McMahon and Cheng, 1990), animals vary stance leg stiffness to regulate running speed. Thus, there is a need for the controller to change the effective leg compliance as a function of speed. This is achieved by adding an additional term $\Delta\gamma^{sc}_{k_{\rm vc}}$ to $\gamma^{sc}_{k_{\rm vc}}$ computed in (25), where,

$$\Delta\gamma^{sc}_{k_{\rm vc}} := \begin{cases} -K_{k^{sc}_{\rm vc}}\sqrt{\Delta\dot{p}^{h,avg}_{\rm hip}}, & \Delta\dot{p}^{h,avg}_{\rm hip} > 0 \\ 0, & otherwise \end{cases}, \quad (31)$$

with, $\Delta\dot{p}^{h,avg}_{\rm hip} = (\dot{p}^{h,avg}_{\rm hip} - \dot{p}^{h,avg*}_{\rm hip})$, and $\dot{p}^{h,avg*}_{\rm hip}$, $\dot{p}^{h,avg}_{\rm hip}$ being the nominal and last step average horizontal hip speeds respectively.

Finally, to enable large touchdown angles at faster speeds to effectively slow down the robot and to prevent large touchdown angles at slow speeds from causing the foot to slip, the β-parameters are bounded, such that, $-\beta^{sat} \le \beta \le \beta^{sat}$, with the saturation for the β-parameter corresponding to touchdown, β_{TD}, specified as a function of speed, as below,

$$\beta^{sat}_{TD} = \begin{cases} 2^\circ, & 0 \le \dot{p}^{h,avg}_{\rm hip} < 1.2 \\ 1.5^\circ, & 1.2 \le \dot{p}^{h,avg}_{\rm hip} < 1.7 \\ 2^\circ, & 1.7 \le \dot{p}^{h,avg}_{\rm hip} < 2 \\ 2.5^\circ, & 2 \le \dot{p}^{h,avg}_{\rm hip} < 2.5 \\ 4^\circ, & 2.5 \le \dot{p}^{h,avg}_{\rm hip} \end{cases} \quad (32)$$

Modifications to account for the passive feet: The softer impacts due to the feet in the shoes result in the spring not compressing sufficiently and cause flight phases with smaller durations and with lower ground

clearance. To account for the softer impacts, the nominal virtual compliance, $k_{\rm vc}^*$, was reduced by 18%.

During stance-decompression, energy injection causes the spring to compress initially and then rapidly decompress resulting in rapid knee extension causing push off. However, due to the geometry of the passive foot—specifically, the absence of an ankle rotation DOF—when the leg is backward at the beginning of stance-decompression, only the forward part of the shoe is in contact with the ground. This causes a significant fraction of the injected energy not to be translated to a push off; rather it rapidly affects the angle of the foot with respect to the ground. This effect is more pronounced when the spring is close to its rest position. To address this, the stance compression-to-decompression switching surface is modified to ensure that switching occurs when the spring is sufficiently compressed,

$$\mathcal{S}^{exp}_{sc\to sd} := \mathcal{S}_{sc\to sd} \cap \{x_{\rm s} \in TQ_{\rm s} \mid \theta_{\rm s} > \theta_{50\%},\ q_{{\rm Bsp}_{\rm st}} < 20^\circ\}, \tag{33}$$

where, $\theta_{50\%}$ is the value of $\theta_{\rm s}$ at 50% into stance.

To prevent (a) slipping towards the end of stance when the stance forces are small, (b) hyper-extension of the heavy shin, and (c) large vertical velocities at liftoff, the stance-decompression to flight switching surface is modified as below,

$$\begin{aligned}\mathcal{S}^{exp}_{sd\to {\rm f}} := \mathcal{S}_{sd\to {\rm f}} \cap \{x_{\rm s} \in TQ_{\rm s} \mid q_{{\rm Bsp}_{\rm st}} < 15^\circ,\\ q_{{\rm LS}_{\rm st}} < 2^\circ\} \cap \{x_{\rm s} \in TQ_{\rm s} \mid \dot{p}^v_{\rm hip} > \dot{p}^{v,s-*}_{\rm hip}\},\end{aligned} \tag{34}$$

where, $\dot{p}^v_{\rm hip}$ is the vertical hip velocity, and $\dot{p}^{v,s-*}_{\rm hip}$ is the nominal liftoff vertical hip velocity.

Finally, to prevent the shoes from scuffing the ground during leg swing, the swing leg shape virtual constraint is modified to fold the leg by an additional constant amount.

Modifications to account for unmodeled cable stretch in leg angle transmission: The running controller accounts for unmodeled cable stretch in the leg shape coordinates, but not the leg angle coordinates. During the stance-decompression phase, the nominal virtual constraint specifies the torso to pitch backward. In experiments, the torso is sometimes driven forward to correct tracking errors, which results in forward pitching during flight causing a significant torso error on impact. To prevent this, when the torso velocity drops below a threshold, the controller for the torso pushes the torso backward instead of enforcing the virtual constraint.

On initiation of the flight phase, the event-based controller $\Gamma^{\alpha_c}_{\rm f}$ ensures hybrid invariance through the correction polynomials, $h^{\rm f}_c$ as in (15), such that the modified virtual constraints smoothly join the nominal ones half-way into the flight phase. During experiments, large errors at liftoff may cause the modified virtual constraint to initially reverse the direction of motion, resulting in significant leg angle cable stretch and subsequent large touchdown errors. To handle this, the correction polynomials are modified such that the modified virtual constraint smoothly joins the nominal one at an adaptively chosen location that is either 50%, 75%, or 95% into the flight phase, depending on the sign and magnitude of the error on transition to flight.

With these modifications, the running experiments with passive feet can be performed. The walking controller of (Sreenath et al., 2011b) is employed, along with a torso offset to lean the torso forward to induce stable walking with the passive feet at 1.26 m/s. The walking-to-running transition controller developed in section V-A is used to excite running. On transition, the modified controller described above is executed to sustain running at an average speed of 1.07 m/s obtaining 100 running steps. Figure 11(b) illustrates snapshots of a typical running step. The average stance and flight times are 360 ms and 151 ms, respectively, i.e. flight amounts for 30% of the gait. The ground clearance is approximately 2 inches (5 cm) and the specific cost of mechanical transport (c_{mt}) is 0.75. Figure 12(b) depicts the mean joint angles and motor torques, normalized over time, for 50 consecutive steps of running. Figures 13(b), 14(b) illustrate the β and γ-parameters.

Appendix B
Analyzing Stability of Γ^γ Controller

To analyze stability, the Poincaré map is numerically computed. To ease computation, the section $\tilde{\mathcal{S}}_\gamma = \{x_s \in TQ_s \mid \theta_s = \theta_{77\%}\}$ will be considered instead of $\mathcal{S}_\gamma$; $\tilde{\mathcal{S}}_\gamma$ represents a switching surface 77% into the stance phase. We can then study the eigenvalues of the Poincaré map $\tilde{P}_\gamma : \tilde{\mathcal{S}}_\gamma \times \mathcal{B} \times \mathcal{G} \to \tilde{\mathcal{S}}_\gamma$. Note that, while the Poincaré section $\tilde{\mathcal{S}}_\gamma$ is used instead of $\mathcal{S}_\gamma$, the β, γ parameters still continue to be updated on their respective switching surfaces $\mathcal{S}_\beta$ and $\mathcal{S}_\gamma$. To define the Poincaré map $\tilde{\mathcal{P}}_\gamma$, we define three maps: $\tilde{P}^1_\gamma : \tilde{\mathcal{S}}_\gamma \times \mathcal{B} \times \mathcal{G} \to \mathcal{S}_\gamma$ which maps a state on $\tilde{\mathcal{S}}_\gamma$ along with β and γ to the post-impact surface, which is also the switching surface $\mathcal{S}_\gamma$ for the event-based controller Γ^γ; $\tilde{P}^2_\gamma : \mathcal{S}_\gamma \times \mathcal{B} \times \mathcal{G} \to \mathcal{S}_\beta$ which maps a state on $\mathcal{S}_\gamma$ to the stance-compression to stance-decompression transition surface, which is also the switching surface $\mathcal{S}_\beta$ for the event-based controller Γ^β; and finally $\tilde{P}^3_\gamma : \mathcal{S}_\beta \times \mathcal{B} \times \mathcal{G} \to \tilde{\mathcal{S}}_\gamma$, which maps a state on $\mathcal{S}_\beta$ back to $\tilde{\mathcal{S}}_\gamma$, the Poincaré section under consideration. To further clarify this, we define,

$$x^a_p[k] = \tilde{\mathcal{P}}^1_\gamma(x_p[k], \beta[k], \gamma[k]) \tag{35}$$

$$x^b_p[k] = \tilde{\mathcal{P}}^2_\gamma(x^a_p[k], \beta[k], \Gamma^\gamma(x^a_p[k])). \tag{36}$$

Then,

$$\begin{aligned} x_p[k+1] &= \tilde{\mathcal{P}}_\gamma(x_p[k], \beta[k], \gamma[k]) \\ &= \tilde{\mathcal{P}}^3_\gamma\left(x^b_p[k], \Gamma^\beta(x^b_p[k]), \Gamma^\gamma(x^a_p[k])\right) \end{aligned} \tag{37}$$

Thus the γ parameters continue to be updated on the switching surface $\mathcal{S}_\gamma$, while the β parameters are updated on the switching sruface $\mathcal{S}_\beta$. The switching section $\tilde{\mathcal{S}}_\gamma$ serves only to define the Poincaré map $\tilde{\mathcal{P}}_\gamma$. With this, the eigenvalues of the linearized Poincaré map was computed and a dominant eigenvalue of magnitude 0.6072

TABLE III
GLOSSARY OF SYMBOLS.

Symbol	Description
α_p	Coefficients for Bézier polynomial for $p \in \mathcal{P}$
α_p^c	Coefficients for correction polynomial for $p \in \mathcal{P}$
α_{vc}	Parameter vector for the virtual compliant element
β	Parameter vector for Γ^β controller
γ	Parameter vector for Γ^γ controller
$\Delta_{\mathrm{s}\to\mathrm{f}}$	Stance to flight impact map
$\Delta_{\mathrm{f}\to\mathrm{s}}$	Flight to stance impact map
Γ_p^α	Continuous-time controller for $p \in \mathcal{P}$
Γ^β	Discrete-time controller for hybrid invariance
Γ^γ	Discrete-time controller for robustness
B_e	Input matrix for unconstrained dynamics
C_e	Coriolis matrix for unconstrained dynamics
D_e	Inertia matrix for unconstrained dynamics
$F^N_{\mathrm{toe_{st}}}$	Stance toe normol ground reaction force
$f_{\mathrm{s}}, f_{\mathrm{f}}$	Drift vector field for stance, flight dynamics
G_e	Gravity matrix for unconstrained dynamics
$g_{\mathrm{s}}, g_{\mathrm{f}}$	Input vector field for stance, flight dynamics
$g_{\mathrm{mLS_{st}}}$	Input vector field for stance motor leg shape input
H_0^p	Controlled variable selection matrix for $p \in \mathcal{P}$
h_p	Virtual constraints for $p \in \mathcal{P}$
h_d^p	Desired evolution of virtual constraints for $p \in \mathcal{P}$
h_c^p	Correction terms for virtual constraints for $p \in \mathcal{P}$
$\mathcal{P} = \{\mathrm{s}, \mathrm{f}\}$	Represents the stance, flight phase set
P_β	Poincaré map for Γ^β controller
P_γ	Poincaré map for Γ^γ controller
$p^h_{\mathrm{hip}}, p^v_{\mathrm{hip}}$	Horizontal and vertical position of the hip
$p^v_{\mathrm{toe_{sw}}}$	Vertical position of swing toe
Q_e	Unconstrained / extended configuration space
Q_{s}	Stance configuration space
Q_{f}	Flight configuration space
$q_e, q_{\mathrm{s}}, q_{\mathrm{f}}$	Generalized coordinate vector in $Q_e, Q_{\mathrm{s}}, Q_{\mathrm{f}}$
$q_{\mathrm{LA_{st}}}$, $q_{\mathrm{LA_{sw}}}$	Leg angle coordinate for stance, swing leg
$q_{\mathrm{LS_{st}}}$, $q_{\mathrm{LS_{sw}}}$	Leg shape coordinate for stance, swing leg
$q_{\mathrm{mLS_{st}}}$, $q_{\mathrm{mLS_{sw}}}$	Leg angle motor angle for stance, swing leg
$q_{\mathrm{Bsp_{st}}}$, $q_{\mathrm{Bsp_{sw}}}$	$\mathrm{B_{spring}}$ pulley angle for stance, swing leg
q_{Tor}	Torso angle
$\mathcal{S}_\beta$	Poincaré section for P_β
$\mathcal{S}_\gamma$	Poincaré section for P_γ
$\mathcal{S}_{\mathrm{s}\to\mathrm{f}}$	Stance to flight switching surface
$\mathcal{S}_{\mathrm{f}\to\mathrm{s}}$	Flight to stance switching surface
$TQ_{\mathrm{s}}, TQ_{\mathrm{f}}$	Tangent bundle for stance, flight
$\mathcal{U}$	Input set
u	Input vector
$u_{\mathrm{mLS_{st}}}$	Stance motor leg shape torque
$\tilde{u}$	Actuators used to enforce stance virtual constraints
u_p^*	Input that renders $\mathcal{Z}_{\alpha_p}$ invariant for $p \in \mathcal{P}$
$x_{\mathrm{s}}, x_{\mathrm{f}}$	State vector for stance, flight dynamics
$x_{\mathrm{s}}^-, x_{\mathrm{f}}^-$	Pre-transition stance, flight state
$x_{\mathrm{s}}^+, x_{\mathrm{f}}^+$	Post-transition stance, flight state
y_p	Virtual constraints for $p \in \mathcal{P}$
y_p^c	Virtual constraints with corrections for $p \in \mathcal{P}$
$\mathcal{Z}_{\alpha_p}$	Zero dynamics surface for $p \in \mathcal{P}$
z_p	State on zero dynamics surface for $p \in \mathcal{P}$

was obtained indicating that the closed-loop system still remains exponentially stable.